AGU PUBLICATIONS

JGR

Journal of Geophysical Research: Solid Earth

RESEARCH ARTICLE
10.1002/2016JB012839

Key Points:
- Developed new GNSS/GPS velocity field for the Sichuan Province corrected for postseismic transients
- Revised kinematics of the Sichuan Province and resolve two minor blocks with new GNSS/GPS data
- New spatial constraints on postseismic deformation after the Wenchuan earthquake using GNSS/GPS data

Supporting Information:
- Supporting Information S1
- Data Set S1

Correspondence to:
X. Rui,
xurui_3@163.com

Citation:
Rui, X., and D. S. Stamps (2016), Present-day kinematics of the eastern Tibetan Plateau and Sichuan Basin: Implications for lower crustal rheology, *J. Geophys. Res. Solid Earth*, *121*, 3846–3866, doi:10.1002/2016JB012839.

Received 20 JAN 2016
Accepted 20 APR 2016
Accepted article online 22 APR 2016
Published online 14 MAY 2016

Present-day kinematics of the eastern Tibetan Plateau and Sichuan Basin: Implications for lower crustal rheology

X. Rui[1] and D. S. Stamps[2,3]

[1]Sichuan Earthquake Bureau, Research Institute of Disaster Reduction and Emergency Rescue, Chengdu, Sichuan, China, [2]Virginia Tech, Department of Geosciences, Geodesy and Tectonophysics Laboratory, Blacksburg, Virginia, USA, [3]Department of Earth, Planetary, and Space Sciences, University of California, Los Angeles, California, USA

Abstract The Sichuan Province comprises the cratonic Sichuan Basin and the eastern Tibetan Plateau separated by the recently activated Longmen Shan fault zone, thus providing a natural laboratory to study interseismic and postseismic processes. In this work we compute a new regional geodetic velocity solution from most of the continuous Global Navigation Satellite Systems (GNSS)/GPS data available in the Sichuan Province that we assess for transient postseismic deformation. For 11 continuous sites in close proximity to the Wenchuan 2008 event epicenter that were operational during the Wenchuan event we find an average short-term relaxation time of 11 days with maximum amplitude of 6.6 mm for the postseismic transient and no resolvable long-term transient. Using tests for block rigidity guided by previous kinematic studies we elucidate a longer-term transient in GNSS/GPS observations collected after the Wenchuan event that spans an extensive region of the eastern Tibetan Plateau. We correct for transients, produce an updated secular velocity field, and revise the kinematics of the region using elastic block modeling. Our results indicate that predicted slip rates are in good agreement with both geological and GNSS/GPS velocity profile-derived results, and we resolve two independent blocks with the expanded GNSS/GPS data set. Our constraints on the spatial extent of long-term postseismic deformation support models of ductile lower crust in the eastern margin of the Tibetan Plateau.

1. Introduction

The Longmen Shan mountain range is a central feature in the Sichuan Province; their origin has been debated for decades. In one view the mountain range arises from lower crustal material extruding away from the central Tibetan Plateau generating buoyant uplift adjacent to the Sichuan Basin (Figure 1) [*Royden et al.*, 1997; *Clark et al.*, 2005; *Medvedev and Beaumont*, 2006]. An alternative mechanism for the Longmen Shan mountain growth is crustal thickening through thrust faulting on deeply rooted faults [i.e., *Tapponnier et al.*, 2001]. Recent seismic activity along the Longmen Shan (LMS) fault zone has reinvigorated this long-standing debate with new seismic, geodetic, and geologic data lending evidence to support both hypotheses [i.e., *Shen et al.*, 2009; *Hubbard and Shaw*, 2009; *Huang et al.*, 2014; *Liu et al.*, 2014].

Prior to the 12 May 2008 Wenchuan M_s 8.0 earthquake shortening across the LMS was measured at $<$3 mm/yr [*King et al.*, 1997; *Chen et al.*, 2000; *Zhang et al.*, 2004; *Shen et al.*, 2005; *Gan et al.*, 2007]. These data indicated limited shortening and supported the lower crustal flow hypothesis for mountain building along the LMS because the crustal thickening model requires coupled uplift and shortening. However, new geodetic observations related to the Wenchuan event [e.g., *Zhang*, 2008; *Shen et al.*, 2009; *Ding et al.*, 2013; *Huang et al.*, 2014] and the later M_s 7.0, 20 April 2014 Lushan event [*Wu et al.*, 2013; *Jiang et al.*, 2014] measure the process of active shortening from coseismic displacements and postseismic displacements near the LMS up to 2 years after the events. Seismic tomography data [*Liu et al.*, 2014; *Pei et al.*, 2014] and an apparent gap in seismic activity between the Lushan and Wenchuan epicenters [*Li et al.*, 2013] provide evidence in support of a complex geodynamic region at the eastern margin of the Tibetan Plateau where both lower crustal flow and crustal shortening processes drive deformation.

In this work we investigate intraplate deformation at one of Earth's premier locations for studying rheological contrasts in the lithosphere—the Sichuan Province. We calculate a Global Navigation Satellite Systems (GNSS)/GPS velocity field corrected for postseismic transient deformation using newly available continuous and episodic GNSS/GPS data spanning 2008–2015. We combine this velocity

solution with interseismic velocities prior to the Wenchuan earthquake [*Zhang et al*., 2013] to provide an augmented secular velocity solution for the eastern Tibetan Plateau and Sichuan Basin as a contribution to the broader geophysical community. We then use it to revise the kinematics of the Sichuan Province providing new estimates of long-term slip rates on the Longmen Shan and surrounding active faults and resolve two new minor blocks. The new kinematic model predicts fault slip rates that agree well with both geological and GNSS/GPS velocity profile-derived results. Results from isolating postseismic transient deformation elucidates a broad region in the eastern margin of the Tibetan Plateau undergoing transient, postseismic deformation that is consistent with models of lower crustal flow and supports extrusion tectonic hypotheses.

2. Tectonic Setting of the Sichuan Province

The prominent geographic feature in the Sichuan Province is the largest topographic gradient (~5700 m) in eastern Eurasia where the ~330 km Longmen Shan (LMS) fault zone [e.g., *Liu-Zeng et al*., 2009; *Shen et al*., 2009; *Xu et al*., 2009; *Zhang et al*., 2010] separates the cratonic Sichuan Basin and the eastern margin of the elevated Tibetan Plateau (Figure 1). The LMS and associated growth of the Longmen Shan mountains are attributed to the evolution of the Tibetan Plateau, which began forming during the late Cenozoic in response to Indian-Eurasian plate collision.

Formation of the Tibetan Plateau generated thickened crust in its center that transitions to thinner crust at the edges of the plateau. The analysis of receiver functions and seismic velocity anomalies indicate that crustal thicknesses range from 53 to 66 km west of the LMS and 40 to 60 km in the Sichuan Basin [*Wang et al*., 2003; *Xu et al*., 2007; *Yao et al*., 2006, 2008; *Laske et al*., 2012]. Seismic studies from *P* wave tomography also reveal that the Sichuan Basin has seismically fast lithospheric structure to ~250 km, which suggests rigid rheology associated with cratonic domain [e.g., *Li et al*., 2008]. Tomographic studies of the Tibetan Plateau and surroundings indicate seismically slow regions that have been attributed to regions of ductile lower crust [i.e., *Li et al*., 2006, 2008]. Magnetotelluric profiles corroborate the hypothesis of rheologically distinct lower crust [*Unsworth et al*., 2005; *Bai et al*., 2010] that, in part, accommodates expansion of the Tibetan Plateau.

Eastward expansion of the Tibetan Plateau is also accommodated by several highly active major faults that bound an amalgamation of crustal blocks. Geodetic and seismic data observe strain partitioning by left-lateral strike slip along the Xianshuihe, Kunlun, Anninghe, and Zemuhe faults and right-lateral strike slip along the Red River and Longriba faults. Historically, and at present, large-magnitude compressional and strike-slip events with voluminous low-magnitude earthquakes pervade the western and southeastern Sichuan Province [*Zhang et al*., 2010, and references therein]. The Sichuan Basin has been isolated from major seismic events and significant crustal deformation due to its thickened cratonic lithosphere. Prior to the 2008 Wenchuan event, rates of surface deformation along the LMS were <3 mm/yr [*King et al*., 1997; *Chen et al*., 2000; *Zhang et al*., 2004; *Shen et al*., 2005; *Gan et al*., 2007] with kinematic and geologic observations indicative of compressional stresses near the Beichuan and right-lateral faulting in the northern LMS—consistent with the M_s 8.0 Wenchuan event.

3. GNSS/GPS Data Analysis

The data we process are from three sources: (1) the Sichuan GNSS/GPS Network of the Sichuan Earthquake Bureau, which contain 37 continuous GNSS/GPS sites, with 14 sites spanning January 2004 to August 2015 (11 are in close proximity to the Wenchuan event) and 23 sites that span August 2010 to August 2015; (2) the Crustal Movement Observation Network of China (CMONOC), operated by the China Earthquake Administration and partly maintained by Sichuan Earthquake Bureau. The CMONOC contains 25 continuous GNSS/GPS sites (with 1 site spanning January 2006 to August 2015 and the rest span August 2010 to August 2015) and 542 campaign sites in the region with the new episodic observations in 2009, 2011, 2013, and 2015; and (3) the data from the Sichuan Surveying and Mapping Bureau, which contains 11 continuous GNSS/GPS sites, of which 9 sites were observed at the beginning of 2012 and 2 at the beginning of 2013. Our final velocity solution has transients removed from the new GNSS/GPS stations and will then be merged with the secular velocity solutions

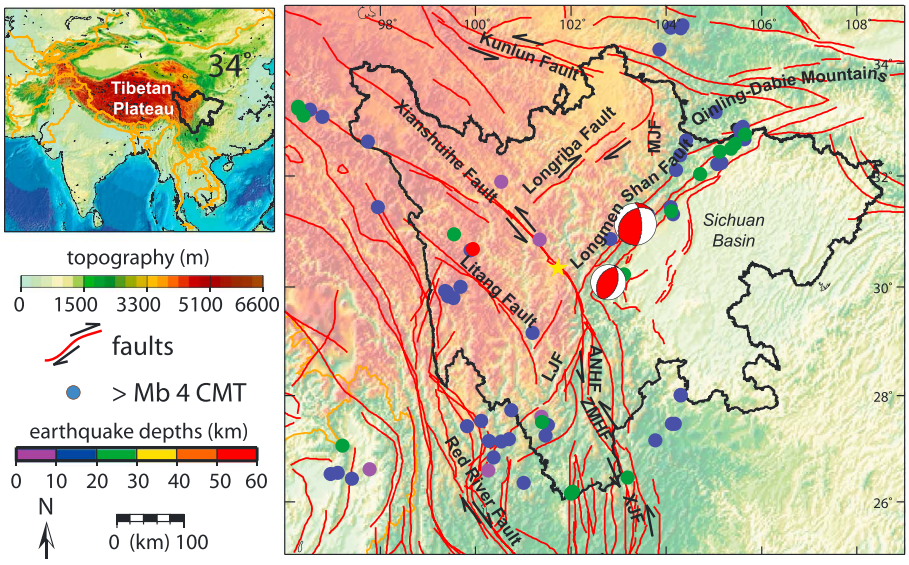

Figure 1. Tectonic setting of the Sichuan Province. Black outline defines the political boundaries of the Sichuan Province. Colored circles show the depths of earthquakes $>M_b$ 4 from the CMT catalog [*Dziewonski et al*., 1981; *Ekström et al*., 2012]. The southernmost focal mechanism represents the M_s 7.0 Lushan earthquake, and the northernmost focal mechanism represents the M_s 8.0 Wenchuan event. The yellow star shows the location of the M_s 6.3 Kandding earthquake. Red lines represent the faults (from *Shen et al*. [2005] and *Taylor and Yin* [2010]). The inset map highlights the Tibetan Plateau and location of the Sichuan Province. ANHF = Anninghe Fault; ZMHF = Zemuhe Fault; XJF = Xiaojiang Fault; LJF = Lijiang-Xiaojinhe Fault; MJF = Minjiang Fault.

from *Zhang et al*. [2013] in a consistent reference frame. We remove transient motions by resolving the postseismic decay times (section 4) and removing GNSS/GPS data observed during these time intervals. We test removing data only for the transient decay time and for 9 months of observations after the Wenchuan and Lushan events. The difference between the two solutions is a maximum of 0.9 mm/yr in the east and 1.6 mm/yr in the north components. For the final solution we choose the conservative approach and remove 9 months of data after both seismic events.

We processed the GNSS/GPS data from all sites loosely following the procedures described in *McClusky et al*. [2000] and *McCaffrey et al*. [2007] using the GAMIT-GLOBK GNSS/GPS processing software [*Herring et al*., 2010a, 2010b]. We combine the raw phase observations from the local GNSS/GPS receivers with raw phase observations from 5 to 10 continuous International GNSS Service (IGS) stations to estimate loosely constrained positions, atmospheric parameters, and Earth orientation parameters, each with associated covariance matrices. We then combine these estimates and their covariances as "quasi-observations" [*Dong et al*., 1998] with the estimates and covariances from the Massachusetts Institute of Technology (MIT) global analysis to estimate positions at each epoch. Then, for continuous sites, we aggregate the daily estimates over periods of 7 days to better assess the long-term statistics of the positions (see Figure 2). For the campaign sites we directly use the daily estimate. We combine the position estimates into a cumulative solution to derive site velocities for the episodic and continuous sites separately and then rotate and translate the two solutions into a consistent reference frame with six common IGS sites available in China (0.13 mm/yr RMS fit). We choose to use sites in close proximity to our region of interest for the combination to obtain the most robust regional solution.

Realistic uncertainties for the estimated positions coordinates and velocities are obtained by adding both white and correlated noise to the daily quasi-observations. To do so we first assign 10 mm for the a priori phase error to make coordinate uncertainties approximately realistic with 2 min sampling following *Herring et al*. [2010a]. Second, we remove apparent outliers and down-weight the daily observations for stations and time periods that reflect a higher than average scatter. Third, we add a random-walk component to all continuous stations that we determined using the first-order Gauss-Markov (FOGMEX) algorithm [*Reilinger et al*., 2006; *Ji and Herring*, 2011; *Ji*, 2011]. Finally, we add an estimate for random-walk noise to the campaign data based on the average of all continuous stations (1.0, 1.5, and 9 mm^2/yr for east, north, and up components, respectively).

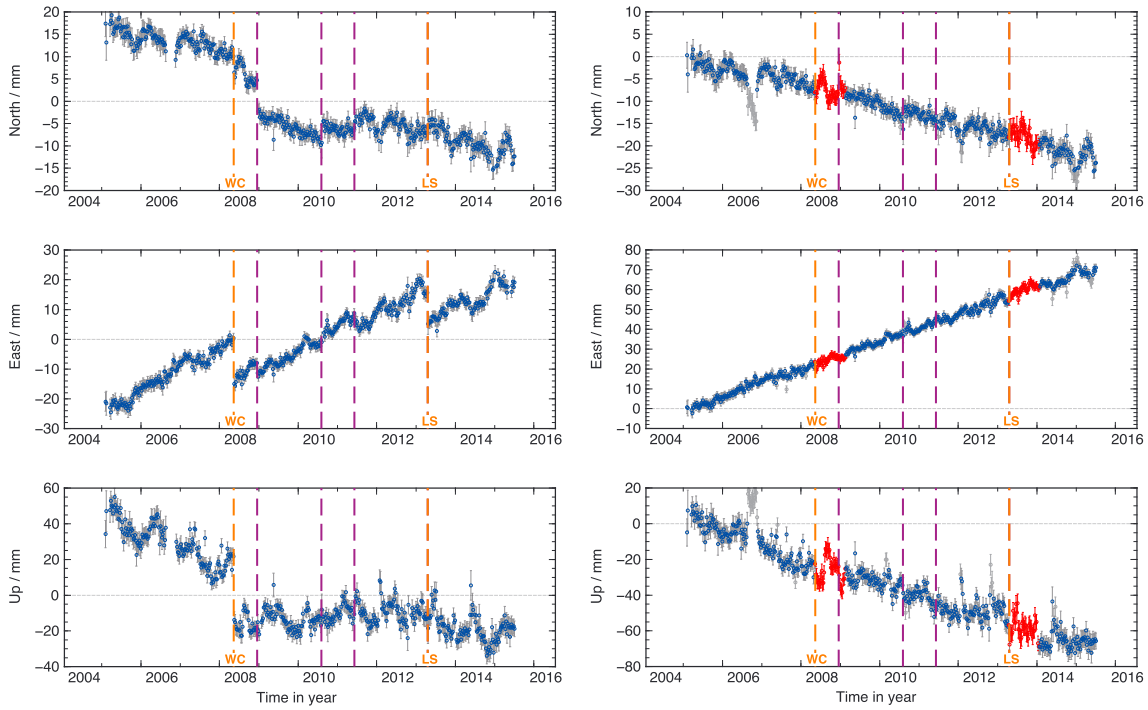

Figure 2. Example of weekly aggregated time series for site QLAI. (left) Uncorrected QLAI time series. (right) QLAI time series corrected for coseismic offsets, offsets due to equipment changes, annual signals, and outliers (in gray). Data that we remove to account for postseismic transients (9 months) is shown in red. Orange lines represent the dates of seismic events (WC for Wenchuan event and LS for Lushan event). Purple lines indicate the antenna change-related breaks. Figure 5a shows the location of QLAI.

To assess whether our noise models describe the error characteristics of the GNSS/GPS observations, we evaluated the normalized root-mean-square (NRMS) and weighted root-mean-square (WRMS) statistics (Figure 3):

$$\mathrm{WRMS} = \sqrt{\frac{N}{N-1}\frac{\sum_{i=1}^{N}\frac{(y_i-(a+bt_i))^2}{\sigma_i^2}}{\sum_{i=1}^{N}\sigma_i^2}}$$

[*Larson and Agnew*, 1991], where y_i is the measured position, N is the number of observations, t represents the time at the ith observations, and the intercept and slope of the best linear fit are a and b, respectively.

Seventy percent of the WRMS scatter is less than 1.7 mm for the north component and 2.1 mm for the east component. The NRMS histograms are approximately normal with a mean value of 0.8 in the north and 1.0 in the east component. These values indicate that our noise models provide a reasonable fit to the error characteristics of the GNSS/GPS measurements [i.e., *McCaffrey et al.*, 2007].

Several episodic GNSS/GPS measurements were obtained within 1 year of the Lushan and/or Kangding events. To mitigate effects from possible coseismic displacements we use seismic intensity distribution maps (Figure S1 in the supporting information) derived from field investigations carried out by the China Earthquake Administration after the Lushan and Kangding earthquakes to determine which campaign sites were likely affected by each earthquake. We remove the epoch nearest spatially to the respective seismic event for campaign sites within the zones of high seismic intensity. We then use WRMS statistics to evaluate the long-term repeatability of daily position estimates and require WRMS <3 mm.

4. Transient Postseismic Deformation

To assess our velocity solution for transient postseismic deformation associated with the Wenchuan and Lushan earthquakes we first evaluate time series for transients from the 11 continuous GNSS/GPS stations operational during both events located along the LMS and within the Sichuan Basin and 18 continuous sites

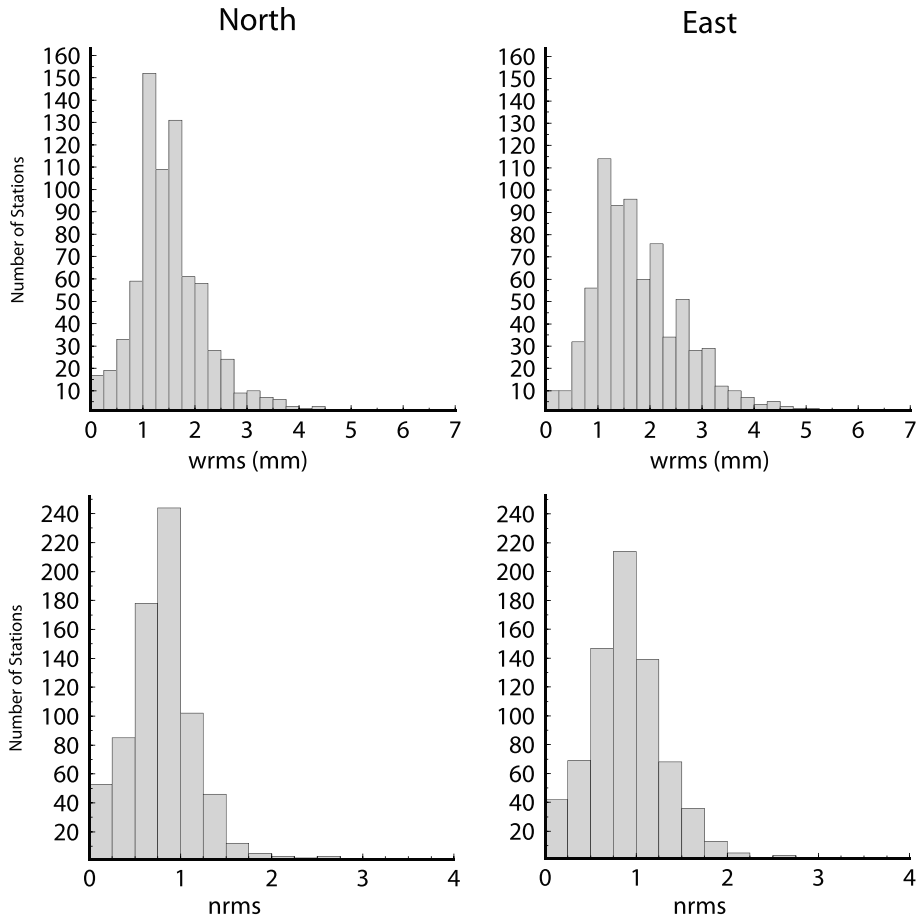

Figure 3. WRMS and NRMS histograms of position estimates.

that observed the Lushan event. We perform an iterative fit to a logarithmic function to estimate the relaxation times and amplitude of transients (Table 1):

$$x(t) = C + \lambda \ln\left(1 + \left(t - t_{\text{eq}}\right)/\tau\right)$$

[e.g., *Savage et al*., 2005], where C is the coseismic offset in meters, t is time in years, τ is the relaxation time in years, and lambda is the amplitude of the logarithmic function. The average relaxation time for north, east, and up components of the continuous time series after the Wenchuan event is 11 days (range 7–18 days; examples in Figures 4a and 4b), which is consistent with *Shen et al*. [2009]. The maximum amplitude of the resolved short-term transient is 6.6 mm (Figure 5). The amplitude of the postseismic transient is largest

Table 1. Results From the Logarithmic Fit to Continuous Time Series in Association With the Wenchuan 2008 Event[a]

Longitude	Latitude	τ	λ_N	λ_E	λ_U	Site	Starting Date
104.06	30.63	8.7	0.70	0.3	1.3	CHDU	16/01/2004
104.54	30.38	7.0	0.50	0.7	0.4	JYAN	03/12/2004
103.75	29.56	9.5	0.30	0.5	0.4	LESH	01/04/2006
104.72	31.43	9.5	1.20	1	1	MYAN	01/04/2006
105.11	29.62	7.3	0.50	1.1	0.3	NEIJ	01/04/2006
103.75	30.91	15.8	0.90	1.3	1	PIXI	15/01/2004
103.30	30.35	10.0	6.60	4.8	0.6	QLAI	01/02/2005
104.10	30.20	9.4	0.40	0.7	0.6	RENS	15/01/2004
104.43	29.45	9.8	0.20	0.4	0.4	ROXI	17/05/2007
103.01	29.98	18.3	0.60	0.2	5.8	YAAN	15/12/2004
104.54	31.00	9.9	0.40	1	0.5	ZHJI	15/01/2004

[a]Tau estimates are in days. Amplitude estimates are in mm.

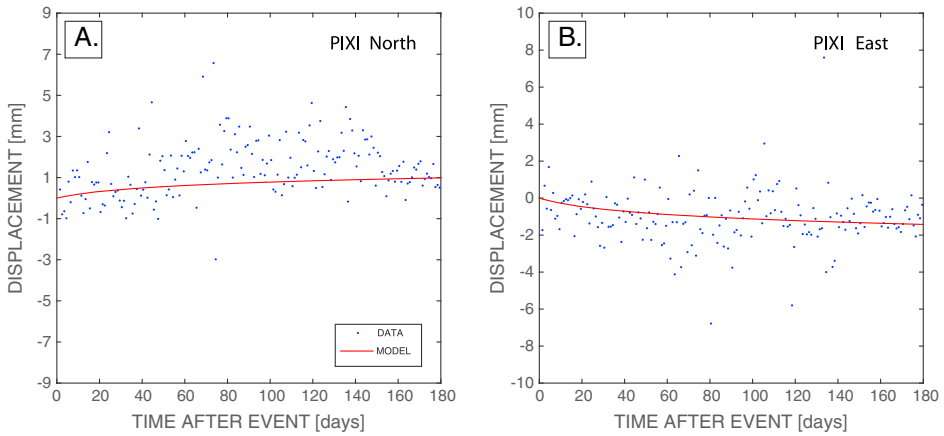

Figure 4. (a) Modeled and calculated time series for the north component of PIXI based on the relaxation times in Table 1 determined using an iterative inversion described in section 4. (b) Same as in Figure 4a but for the east component.

between the epicenters of the Lushan and Wenchuan events in the horizontal components and relatively large near the Lushan event in the vertical component. A long-term transient signal associated with the Wenchuan event may be present in the 11 near-field GNSS/GPS sites, but it is too small to be resolvable with this approach. We are unable to resolve clear short-term or long-term postseismic transients after the Lushan event at the 18 operational continuous sites by fitting the logarithmic function. For the final GNSS/GPS velocity solution we exclude 9 months of data collected after both the Lushan and Wenchuan events. As noted in section 3 we evaluated removing data only for the transient decay times and for 9 months after the Wenchuan and Lushan events with maximum residuals of 0.9 mm/yr in the east and 1.6 mm/yr in the north components. We choose the conservative approach and remove 9 months of data after both events for the final velocity solution.

In a second step we utilize existing secular velocity solutions from *Zhang et al*. [2013] with observations prior to the Wenchuan event for comparison. The *Zhang et al*. [2013] solution includes two velocity fields that we rotate into a consistent, Eurasia reference frame. One solution is comprised of 636 velocities merged from papers published between 2000 and 2008 and is called "merged." The other is comprised of 281 velocities from the CMONOC (1997–2009), the Sichuan GNSS/GPS network (2005–2009), and a campaign 973 project (2005–2009) and named "Chinese." The two velocity solutions largely overlap in the study area. To combine them, we first rotate and translate the merged velocity solution into a consistent reference frame of the Chinese velocity solution using 100 common sites with a resulting RMS fit of 0.38 mm/yr. Co-located sites from the merged and Chinese are consistent within 2 mm/yr. We average the velocities for the common sites and refer to this combined solution as the Zhang solution.

In this second step we calculate the residual velocities at common sites between our new postseismic velocities and the Zhang solution. There are 64 common sites between the velocity solutions based on new data and the Zhang solution. We use 38 of these sites that are located outside of the eastern Tibetan Plateau but

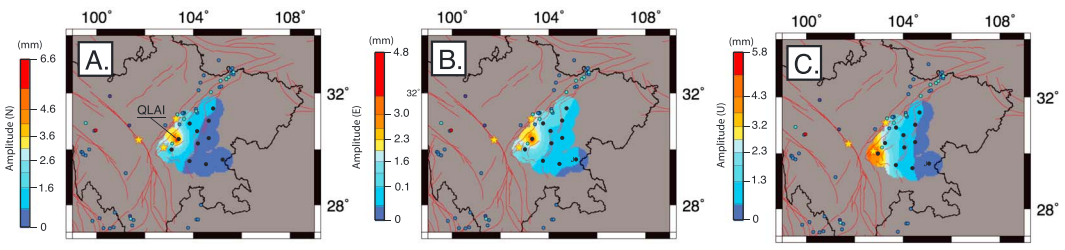

Figure 5. (a) Amplitude of short-term postseismic transient detected after the Wenchuan 2008 event in the north component. Black circles represent the location of each GNSS/GPS station. QLAI shown in Figure 2 is demarcated. A 50 km radius is plotted around the location of the 11 continuous GNSS/GPS sites operational during the Wenchuan event available for this study. (b) Same as in Figure 5a but for the east component. (c) Same as in Figure 5a but for the up component. Colored circles represent the earthquakes as described in Figure 1. Yellow stars represent the Kangding, Lushan, and Wenchuan earthquakes from west to east, respectively.

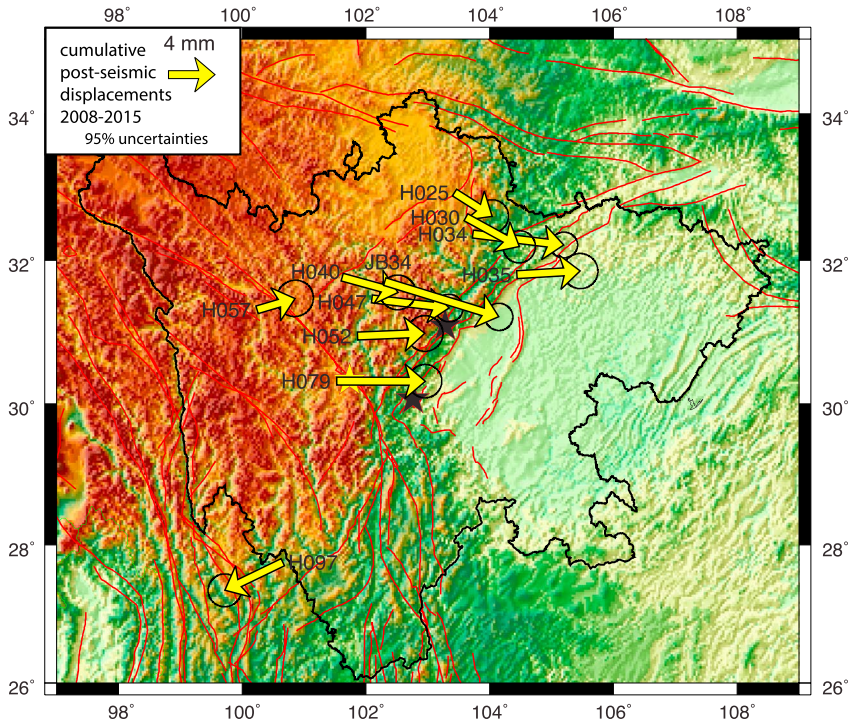

Figure 6. Cumulative postseismic surface displacements detected using the methods described in section 4.

within China to rotate the disparate velocity solutions into a consistent reference frame (RMS = 0.45 mm/yr). As with the combination described in section 3 we use common sites that are in close proximity to our region of interest. We find that 11 sites with velocity differences >3 mm/yr that we propose are associated with postseismic deformation. All 11 sites are located within the Sichuan Province and distributed within close proximity of the Longmen Shan fault and/or on the eastern margin of the Tibetan Plateau where ductile lower crustal material is hypothesized. There is one exception located outside the southern border of the Sichuan Province. The cumulative transient deformation up to 2015 detected with this approach is shown in Figure 6. The new secular velocity solution corrected for this transient deformation is shown in Figure 7.

In section 5 we describe the kinematic modeling, our approach for detecting postseismic deformation at new continuous GNSS/GPS locations, and the revised long-term kinematics of this region derived from our new secular velocity solution.

5. Kinematic Modeling

Kinematic models are used to test the ongoing debate concerning the deformation behavior of the Tibetan Plateau and surroundings: is surface motion best explained by a continuous, broad distribution [e.g., *Flesch et al.*, 2001; *England and Molnar*, 2005] or by discrete blocks with strain accommodated on distinct, narrow faults [e.g., *Tapponnier et al.*, 2001; *Thatcher*, 2007]? In this work we contribute to the debate by developing a new secular velocity field corrected for transient postseismic deformation that spans 1997–2015, which is then used to constrain the present-day kinematics of the Sichuan Basin and eastern Tibetan Plateau following the methods of *McCaffrey* [2009]. We provide new constraints on long-term fault slip rates and isolate two new blocks with the augmented secular GNSS/GPS velocity solution.

5.1. Previous Kinematic Models

Prior to the Wenchuan 2008 event several authors published tectonic block models that include the eastern margin of the Tibetan Plateau and the Sichuan Basin [e.g., *Shen et al.*, 2005; *Calais et al.*, 2006; *Gan et al.*, 2007; *Loveless and Meade*, 2011; *Zhang et al.*, 2013]. In this work we aim to provide an updated, robust kinematic description of the Sichuan Province; therefore, we use updated block

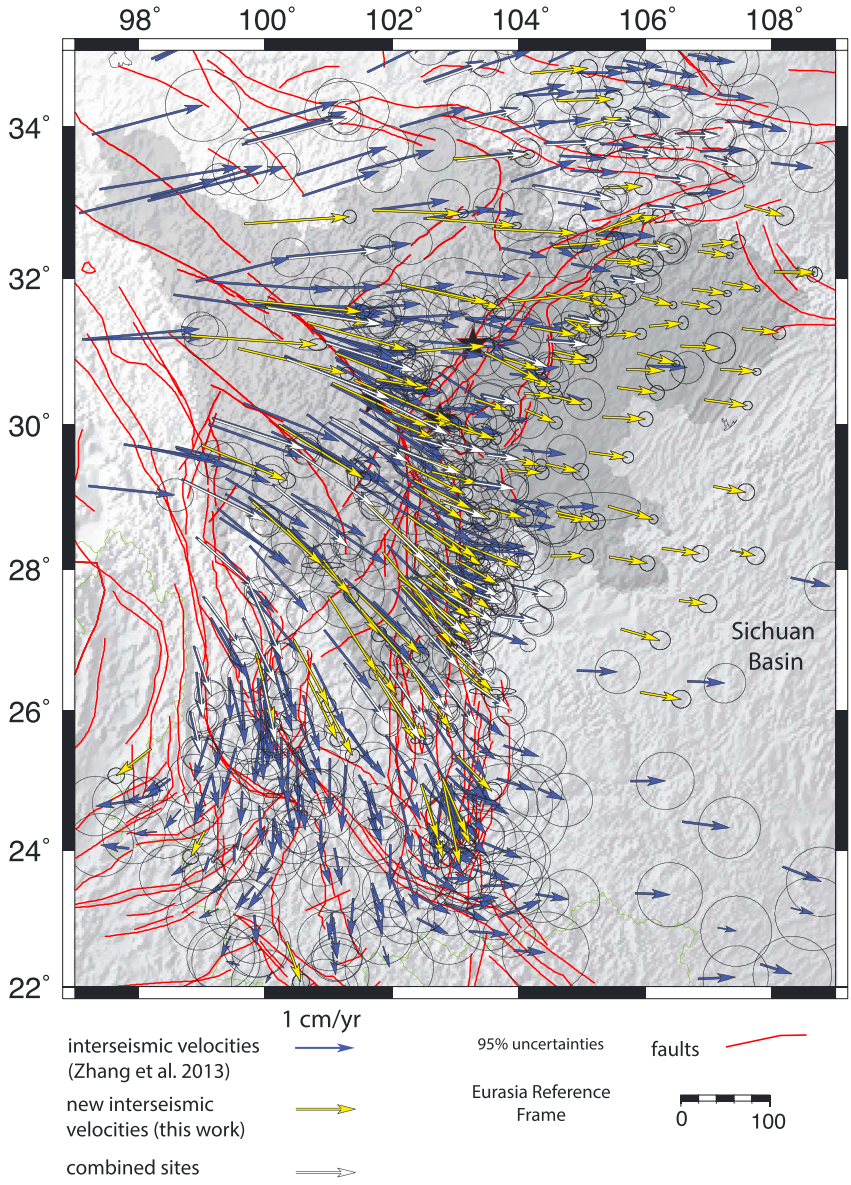

Figure 7. Interseismic (before Wenchuan 2008 event [*Zhang et al.*, 2013]; blue vectors) and new interseismic velocity solution from this work that is comprised of post-Wenchuan episodic GNSS/GPS data and continuous GNSS/GPS data corrected for transient deformation (yellow vectors). White vectors show the combined, common sites. Darker gray region highlights the Sichuan Province with the epicentral location of the Wenchuan 2008 and Lushan 2013 events represented as black stars.

geometries based on *Shen et al.* [2005, 2009], *Meade* [2007], and *Zhang et al.* [2013] that are representative of the range of minor blocks proposed for the Sichuan Province and surroundings.

There are several key differences between these models. *Meade* [2007] divides the Sichuan Province and surroundings into four elastic blocks separated by the locked Longmen Shan (LMS) Fault, Anninghe-Zemuhe Fault, Xianshuihe Fault, and Lijiang-Xiojinhe Fault. *Zhang et al.* [2013] use a similar fault geometry and approach but divide the block west of the LMS with the Minjiang Fault and determine that internal deformation within the blocks is necessary to best fit geodetic velocities on blocks around the Sichuan Basin (south China Block). The block geometry of *Shen et al.* [2005] incorporates the Litang Fault in the western Sichuan Province, which we include and also update with the revised block configuration in *Shen et al.* [2009] by separating the region west of the LMS into two blocks following the Longriba Fault. The Shen model also differs from Meade and Zhang by focusing on rigid

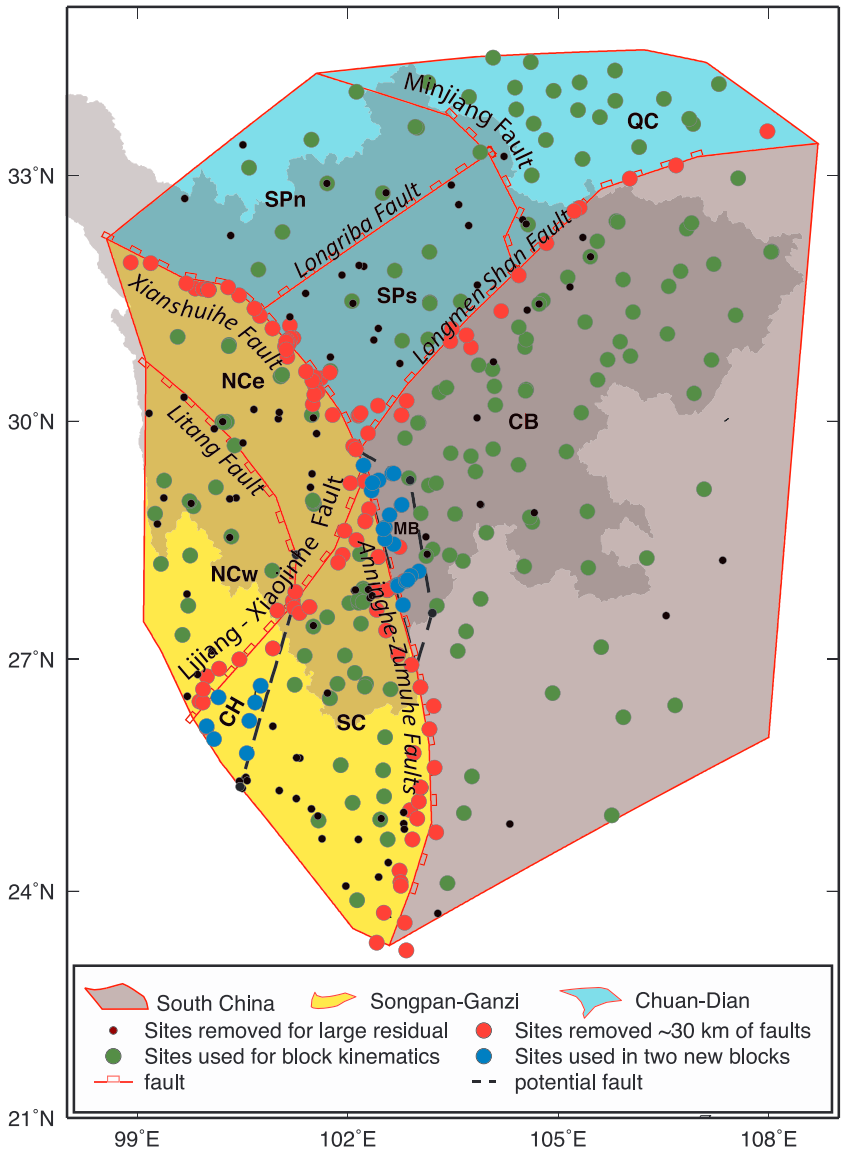

Figure 8. Block boundaries and tectonic regions of the kinematic modeling. South China, Songpan-Ganzi, and Chuan-Dian regions are shown as gray, yellow, and blue regions, respectively. Red circles are the sites removed in the inversions because they are within 30 km of the main faults. Black dots show the sites removed due to large residuals. Dashed lines represent the potentially active faults and boundaries for minor blocks resolved with new data in this study.

block rotations without computing elastic strain accumulation on locked faults and removing GNSS/GPS velocities near active faults.

In all previous kinematic models the strain rates across the LMS were considered small with minimal shortening rates between the eastern margin of the Tibetan Plateau and the Sichuan Basin. Deformation associated with the eastward propagation of Tibetan Plateau bounds the Sichuan Basin in previous models with most strain accommodated along the Xianshuihe and Anninghe-Zemuhe Faults.

5.2. New Kinematic Model

We use TDEFNODE [*McCaffrey*, 2009] to develop our new kinematic model, which is divided into seven discrete rigid subblocks without permanent strain that have freely slipping block boundaries based on a priori knowledge of active faulting and previous studies mentioned in section 5.1. As shown in Figure 8, the Sichuan Province is a region where the Chuan-Dian (NCe, NCw, and SC, yellow background; "Chuan" stands for Sichuan and "Dian" stands for Yunnan in Chinese), south China (CB, light gray background), and Songpan-Ganzi (SPn, SPs, and QC with

green background) regions interact together. Here we focus on the present-day angular rotation of rigid blocks constrained by our revised secular GNSS/GPS velocity solution and neglect elastic strain accumulation along block boundaries. Since elastic deformation mostly takes place within ~30 km of the fault for crustal strike-slip faults [i.e., *Savage and Burford*, 1970], we exclude sites located within ~30 km of the four main faults (Longmen Shan Fault, Anninghe-Zemuhe Fault, Xianshuihe Fault, and Lijiang-Xiojinhe Fault) where the majority of strain in the region is accumulated (Figure 8, red circles). Using the statistical tests below we also include the Longriba, Litang, and Minjiang Faults.

We use a rigorous statistical analysis described below to determine if adding additional blocks to previous defined block geometries is required to best fit the observations. For each inversion, we use only the horizontal components of GNSS/GPS data because of large uncertainties in the vertical component. To evaluate the quality of inversion results, we use three statistics following the methods proposed by *McCaffrey et al.* [2007]. First, we use the reduced χ^2 to measure the goodness of the overall fit between model and observations:

$$\mathcal{X}_n^2 = \left[n^{-1}\sum p_i\right]^{1/2}$$

where n is the degrees of freedom and p is the misfit penalty function (for more details, please refer to Appendix 2 of *McCaffrey* [2005]). Second, we use the probability Q [*Press et al.*, 1989, p. 502] to determine if the resulting chi-square for a given model is due to random chance. We require $Q > 10\%$ and use it to guide an iterative process of removing GNSS/GPS velocities with large residuals. With this process we remove 103 GNSS/GPS sites that are inconsistent with rigid block motions (Figure 8, black dots). Third, we use the F test [e.g., *Stein and Gordon*, 1984] to determine if the data fit is significantly improved by adding additional blocks:

$$F = \frac{\left(\chi_{P_1}^2 - \chi_{P_2}^2\right)/(p_1 - p_2)}{\chi_{P_2}^2/p_2}$$

where p_1 and p_2 denote the degrees of freedom for two models with χ^2 defined above for each model. In this study we use the 95% confidence level to reject the null hypothesis. Only after achieving an acceptable Q value do we use F test statistics.

6. Results

We find that the best fit model gives a fit to the GNSS/GPS data with a reduced $\chi^2 = 0.48$ and $Q = 100\%$. WRMS values are 0.85 mm on average with a range of ±0.2 mm for individual blocks (Table 2). The final model has 325 degrees of freedom (d.f.) from 346 observations and 21 free parameters (three parameters for each of the 7 angular velocity vectors).

6.1. Sichuan Basin–South China Block Reference Frame

The Sichuan Basin is part of the broader, nondeforming south China Block, which is bounded on the west by the Longmen Shan and Anninghe-Zemuhe Faults and on the north by Qinling-Dabie mountains. Our combined secular velocity solution is in a consistent International Terrestrial Reference Frame 2008 (ITRF08) Eurasia reference frame (Figure 7) that, for our kinematic analysis, is transformed into a local Sichuan Basin–south China Block reference frame. The estimated angular velocity pole of the Sichuan Basin–south China Block relative to ITRF08 [*Altamimi et al.*, 2012] Eurasia reference frame is 0.095°/Myr located at 117.83°E and 65.18°N (Table 2).

We assess the noise model for the Sichuan Basin–south China Block sites by checking the ratio of the residual magnitudes and their uncertainties. We compare the ratio of all sites used in our definition of the reference frame with a (2-D) chi-square distribution expected from assuming that the north and east residuals are normally distributed with unit variance. Any values in excess of the expected distribution of normalized residuals imply that uncertainty estimates are conservative (Figure 9). We find that our noise model matches the expected distribution of normalized residuals well with the minor excess of values between 20 and 60% indicating conservative uncertainty estimates.

The transformed GNSS/GPS velocity field with respect to the south China Block is shown in Figure 10, and it clearly highlights the differential motion within the study area, such as (1) the prominent clockwise rotation

Table 2. Statistics and Euler Poles for Best Fit Model in a Sichuan Basin–South China Reference Frame[a] and a Eurasia Reference Frame

					Eurasia Reference Frame						
Block	*N*	NRMS	WRMS	*Q*	Longitude	Latitude	Omega	Sig Omega	Maximum	Minimum	Azimuth
SPs	18	0.713	0.930	95.6	110.40	57.02	0.174	0.286	55.10	1.81	15.04
SPn	20	0.806	1.028	87.8	50.44	80.52	0.140	0.124	67.54	2.08	302.55
CB	158	0.601	0.653	100.0	117.84	65.19	0.095	0.024	14.82	0.93	19.08
SC	58	0.715	0.823	99.9	96.57	22.82	−0.988	0.100	0.92	0.16	231.08
NCe	24	0.722	0.790	97.4	97.82	25.43	−1.593	0.172	0.83	0.14	208.39
NCw	24	0.754	0.855	95.4	95.92	24.77	−1.480	0.203	1.03	0.16	222.75
QC	44	0.727	0.864	99.6	105.16	23.52	−0.378	0.133	5.16	0.49	180.37
SPs[b]	16	1.179	1.195	13.5	105.15	43.47	0.689	0.236	5.70	0.38	10.78
					Sichuan Basin–south China reference frame						
SPs	-	-	-	-	105.04	47.09	0.081	0.307	66.63	4.16	82.67
SPn	-	-	-	-	332.38	54.18	0.064	0.026	101.90	4.77	49.65
SC	-	-	-	-	97.45	26.35	−1.058	0.104	0.64	0.21	190.89
NCe	-	-	-	-	98.35	27.56	−1.665	0.175	0.52	0.16	228.39
NCw	-	-	-	-	96.54	27.10	−1.551	0.206	0.68	0.17	206.28
QC	-	-	-	-	106.46	31.59	−0.453	0.138	1.11	0.48	294.12

[a]*N* is the number of data in the block, twice the number of vectors for GNSS/GPS data; latitude, longitude, omega, sig omega, maximum, minimum, and azimuth give the Euler pole for the block rotation, the uncertainty (°/Ma), and azimuth.
[b]Tests with postseismic velocities as described in section 7.3.

around the eastern Himalayan syntaxis and counterclockwise rotation around Songpan-Ganzi Block; (2) relative motions along Xianshuihe, Anninghe, and Zemuhe Faults; and (3) the abrupt shortening from Songpan-Ganzi region to the south China Block.

6.2. Block Motion

Our best fit model is shown in Figure 11, and the residuals are shown Figure 12. To the first order we find that blocks NCe, NCw, and SC in the Chuan-Dian region rotate fastest with a clockwise motion that is consistent with observed left-lateral strike slip on the Xianshuihe, Anninghe-Zumehe, Litang, and Lijian-Xiaojinhe Faults. The NCe

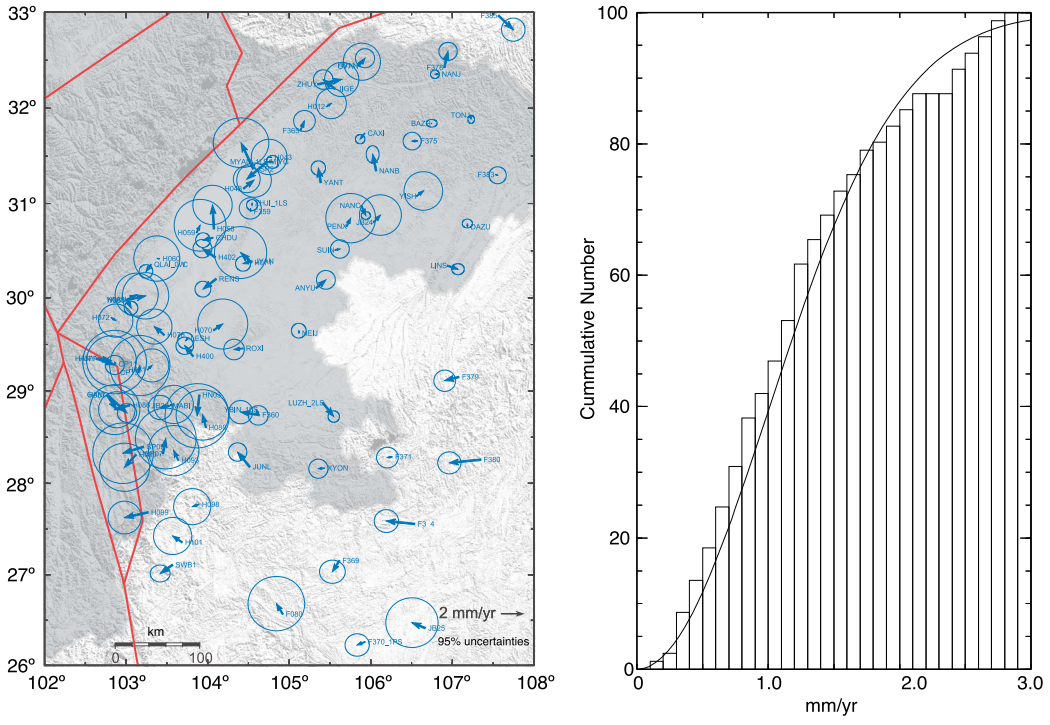

Figure 9. (left) Velocities used in the Sichuan Basin–south China reference frame. (right) Histogram of residuals for sites used to define the Sichuan Basin–south China reference frame.

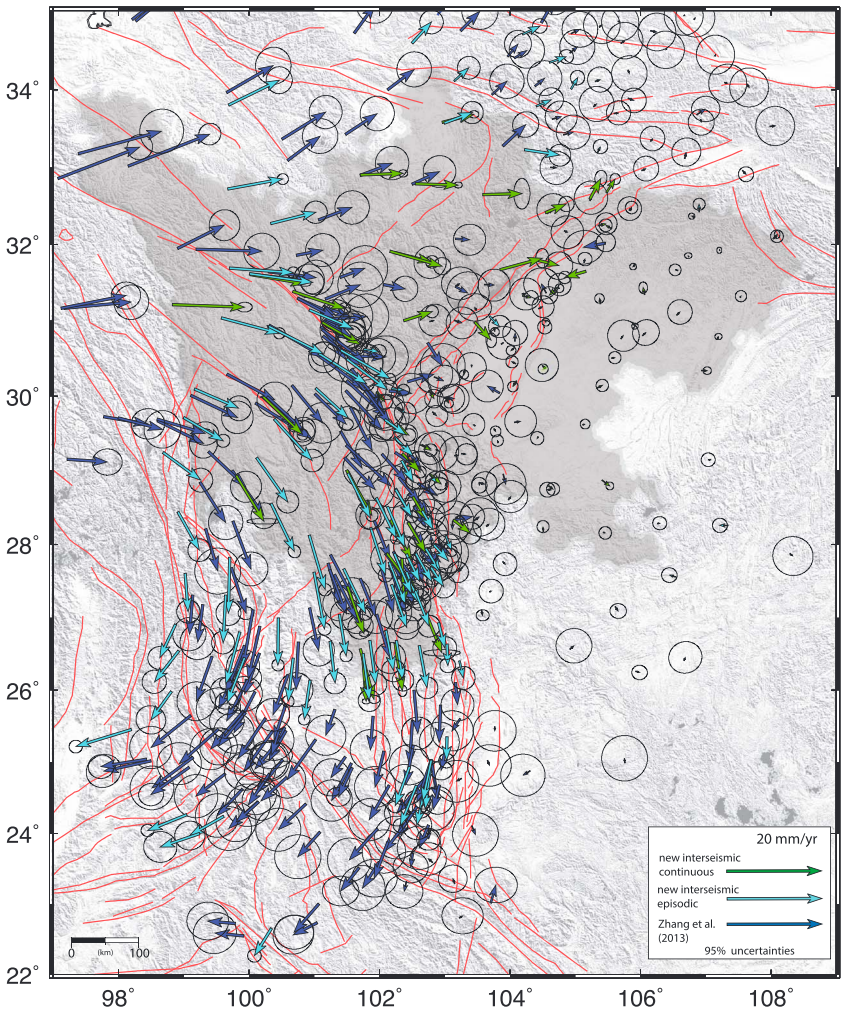

Figure 10. GNSS/GPS velocity field from *Zhang et al.* [2013] (blue vectors), new episodic sites from this study, which include all common sites (cyan), and new continuous GNSS/GPS sites from this study (green vectors) with respect to Sichuan Basin–south China Block reference frame. For clarity, we remove sites that have uncertainties larger than 2 mm/yr in this figure.

and NCw blocks rotate clockwise about Euler poles located at 96° ± 2°E and 25° ± 1°N with rates of −1.6 and −1.5°/Myr, respectively, relative to the Eurasian plate for consistency with previous kinematic studies. Block SC rotates about a Euler pole in close proximity (96.75°E, 22.82°N) but with slower angular velocity of −0.988°/Myr. The relative motion of SC and NCw/NCe (0.5°/Myr) also indicates left-lateral strike motion of bounded Lijiang-Xiaojinhe Fault. The Sichuan Basin-south China Block (CB), SPn, and SPs move with small counterclockwise rotation (0.1°/Myr) with differently located Euler poles. Block QC rotates clockwise at a rate of −0.3°/Myr relative to the Eurasian plate. Block rotations relative the Sichuan Basin–south China Block are in Table 2.

We compare this result with the block kinematic model published by *Shen et al*. [2005] because our methods are closely aligned. We find in our model that the block motions of NCe and NCw separated by the Litang Fault are more consistent in the rotation rate and orientation than that of *Shen et al*. [2005]. Using the augmented GNSS/GPS velocity field the *F* test shows that removing the Litang Fault does not degrade the fit significantly ($P_F = 13.1\%$). Euler pole locations of the Sichuan Basin–south China Block (CB) and the northern Songpan-Ganzi region (SPn) also disagree with *Shen et al*. [2005]. For block CB, both of the results share the similar latitude of the Euler pole, while the longitude of this study is located ~64° westward; thus, it is closer to Sichuan Basin. Block SPn shares the similar longitude with *Shen et al*. [2005], but the latitude of this study is located ~23° southward. We suspect that these inconsistencies are likely due to differences in the distribution of geodetic data available for this work. To eliminate the possibility of model setup as a cause for the differences we reproduce the results of previous kinematic studies in the supporting information.

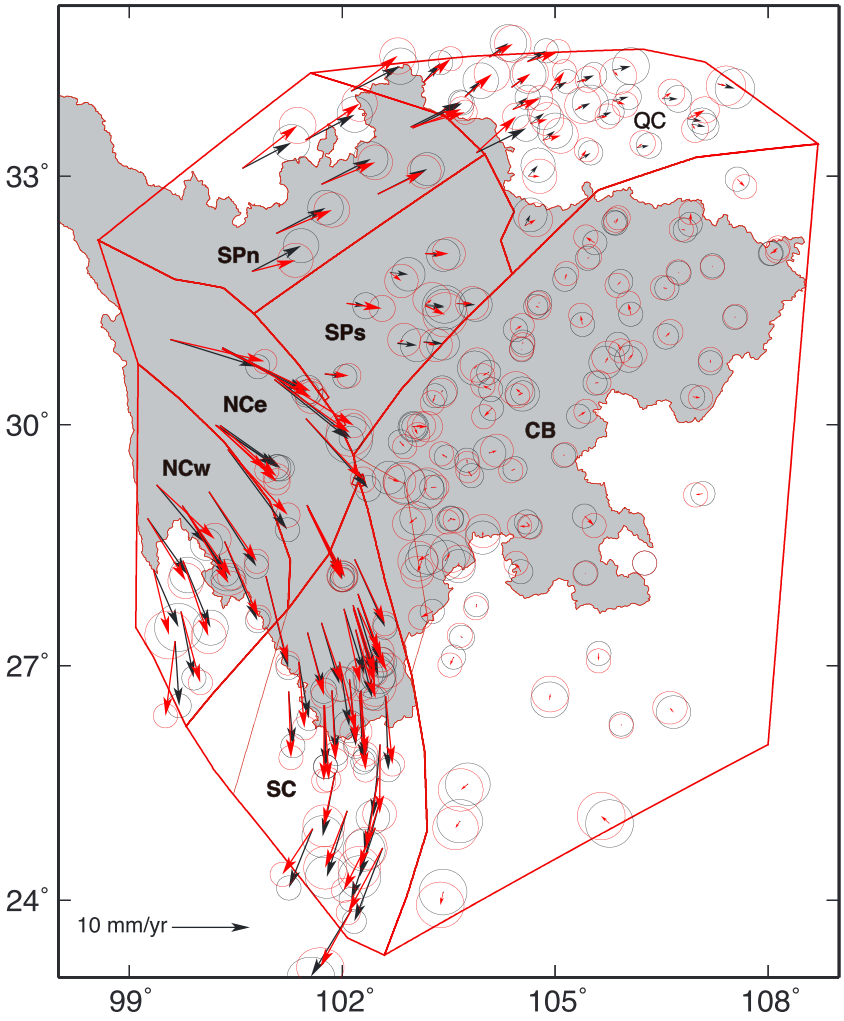

Figure 11. Observed (red arrows) and predicted (black arrows) velocity from the best fit model in a Sichuan Basin–south China Block reference frame.

6.3. Fault Slip Rates

Figure 13 shows the predicted long-term fault slip rates from the best fit model. Clearly, the Xianshuihe and Anninghe-Zemuhe Faults dominate the strike-slip motion within the study area. Even though the maximum left-lateral slip rate of ~20 mm/yr occurs in the northernmost region of this fault at ~30 km, the average left-lateral slip rate on the shallow part (<10 km) of Xianshuihe Fault is 11 ± 1 mm/yr, which is consistent with the previously published GNSS/GPS-derived results [*Shen et al.*, 2005; *Meade*, 2007]. The averaged shallow part slip rate (<10 km) on the Anninghe-Zemuhe Fault is 10.5 ± 0.5 mm/yr. Within the Chuan-Dian region the Lijiang-Xiaojinhe and Litang Faults slip slowly with rates of 3 ± 2 mm/yr and 4 ± 1 mm/yr, respectively. For faults within the Songpan-Ganzi region the predicted long-term slip rates of the Longmen Shan and Longriba Faults are 2 ± 1 mm/yr and 3 ± 1 mm/yr, respectively. Similarly, the average slip rate of the Mingjiang Fault is 2 ± 1 mm/yr; however, the northernmost segment of this fault yields a higher slip rate of 6 ± 3 mm/yr. We suspect that the rapid changes in slip rate on the Mingjiang Fault and Xianshuihe Fault are not realistic, rather an artifact caused by sparse data in this specific area, an oversimplified fault geometry definition, or a boundary effect.

7. Discussion

7.1. Geodetic Versus Geologic Slip Rates

Fault slip rates constrained by GNSS/GPS in a block kinematic model may not represent long-term fault slip rates informed by dating of fault material or the estimated fault slip rates from direct observation from

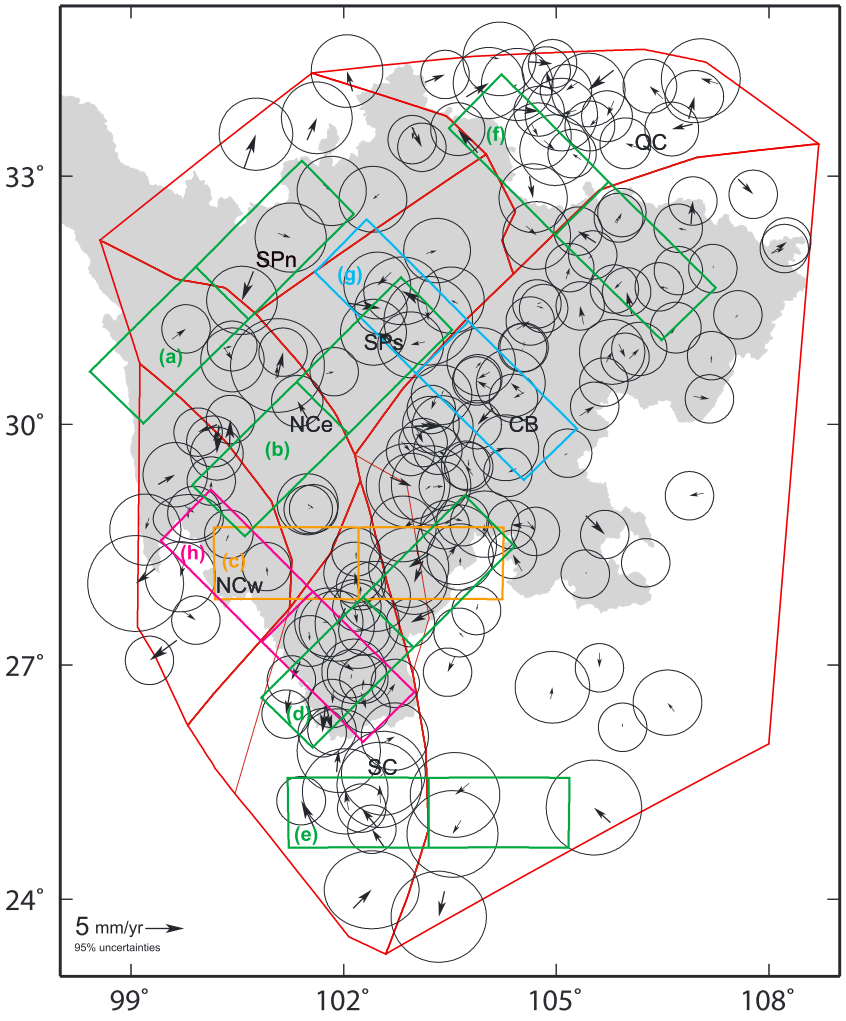

Figure 12. Velocity residuals of the best fit model with 95% uncertainty ellipses.

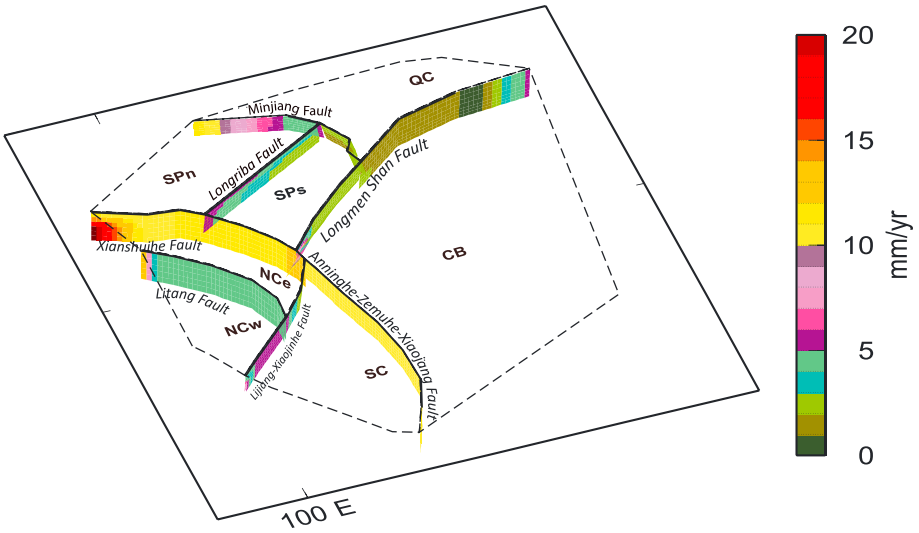

Figure 13. Predicted long-term slip rates of the best fit model.

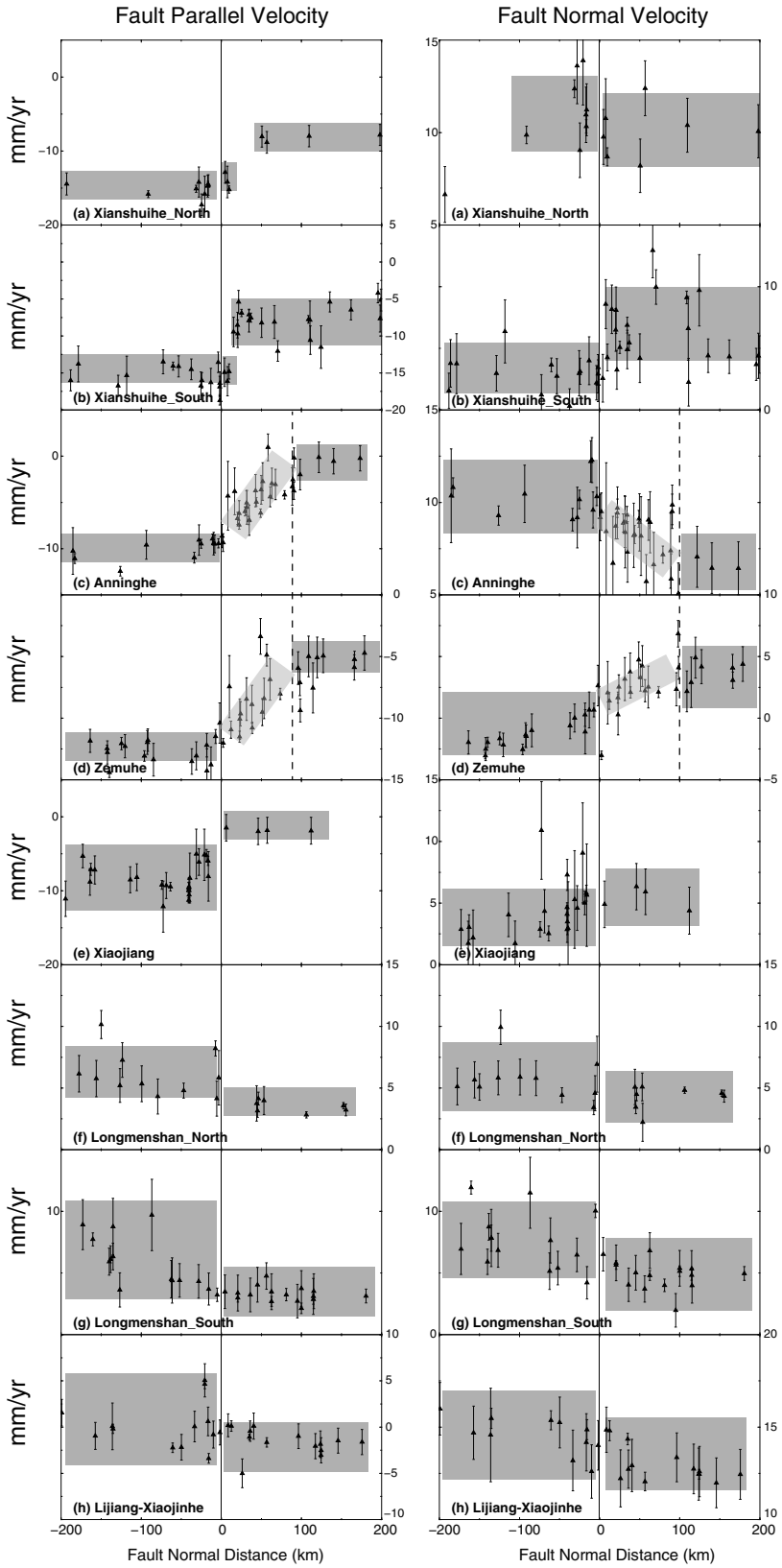

Figure 14. Velocity profile across fault strands as shown in Figure 12. Note that the light gray boxes in Figures 14c and 14b are related to the Daliangshan subblock described in section 7.1, and we use all velocities from our new augmented interseismic velocity solution described in section 3.

Table 3. Comparisons Between Geological Slip Rates, Model-Predicted Long-term Slip Rates, and GNSS/GPS Velocity Profile-Derived Slip Rates

Fault Name	Model-Predicted Slip Rate (This Study)	GPS Velocity Profile-Derived Slip Rate (This Study)	Ranged Slip Rate (Geology)	References (Geology)
Longmen Shan Fault	2 ± 1	1 ± 1	0.0~1.0	*Ma et al.* [2005]; *Densmore et al.* [2007], and *Ran et al.* [2010]
Xianshuihe Fault	11 ± 1	11 ± 2	3.0~20.0	*Wen* [2000], *Zhou et al.* [2001], *Ran and He* [2006], *Qian* [1989], *Li and Du* [1989], *Wang et al.* [2008], *Qian et al.* [1990], *Wen* [1990], *Wen et al.* [1989], *Yi et al.* [2005], and *Li et al.* [1997]
Anninghe Fault	10.5 ± 0.5	8 ± 2	3.0~7.5	*Qian et al.* [1990], *He and Yasutakyr* [2007], *Wen* [2000], *Ran et al.* [2008], *Wang et al.* [1998], *Zhou et al.* [2001], and *Xu et al.* [2003]
Zemuhe Fault	10.5 ± 0.5	8 ± 2	2.5~8.6	*He et al.* [1999], *Du* [2000], *Ren* [1994], and *Ren* [1990]
Xiaojiang Fault	10.5 ± 0.5	7 ± 2	6.0~13.0	*Zhang and Xie* [2001], *He et al.* [2002, 2006], *Wen* [1993], *He et al.* [1993], *Song et al.* [1997], *Shen et al.* [1998], *Shen and Wang* [1999], *Wen et al.* [2007], and *Xu et al.* [2003]
Lijiang-Xiojinhe Fault	4 ± 1	2 ± 2	1.5~5.4	*Xiang et al.* [2002]
Minjiang Fault	6 ± 3	1 ± 1	1~3	*Tang et al.* [2004], *Zhao et al.* [1994], and *Zhou et al.* [2000]
Litang Fault	4 ± 1	2 ± 2	≥1	*Xu et al.* [2005] and *Zhou et al.* [2007]

GNSS/GPS across active faults. In section 6.3 we describe the modeled slip rates based on our new secular velocity solution for the Sichuan Province. Here we calculate the fault slip rates by evaluating GNSS/GPS velocity profiles across fault strands defined in Figure 12 and shown in Figure 14. The regional outline for the profiles are shown in Figure 12 for clarity; however, we use all of the velocities from our new augmented secular velocity solution that are within the bounds of each profile box shown in Figure 7. The starting point of each profile is located in the side where the profile label is pinned (Figure 12). We also compare both estimates of slip rates based on GNSS/GPS observations with geologic slip rates (Table 3).

The GNSS/GPS velocity profiles reveal that the average left-lateral slip rate along Xianshuihe Fault is 11 ± 2 mm/yr, which is consistent with both previously published geodetic [e.g., *Shen et al*., 2005] and geological results [e.g., *Wen et al*., 1989]. About 2 ± 2 mm/yr extension is measured across the southeast segment of Xianshuihe Fault, which is consistent with the geological slip rates reported by *Zhou et al*. [2001]. The Xiaojiang Faults slip left laterally at rates of 7 ± 2 mm/yr, which also agrees with both the geodetic [e.g., *Shen et al*., 2005] and geological results [e.g., *Xu et al*., 2003]. About 3 ± 2 mm/yr extension is measured across the Zemuhe Fault and Xiaojiang Fault. The 3 ± 2 mm/yr compression is measured across the Anninghe Fault, which agrees with the geological result published by *He and Yasutakyr* [2007]. We also find that the velocity profiles across the Zemuhe Fault show that fault-parallel velocities increase smoothly from within block SC to the Zemuhe Fault and then increase abruptly until ~100 km toward block CB (velocity gradient shown in light gray in Figure 14d). The Anninghe Fault parallel velocity profile shows a similar trend (see Figure 14c). Such information implies that between CB and SC there is a separate and ~100 km wide deformation zone which, according to a geological report [e.g., *Wen et al*., 2013], is named Daliangshan subblock. The Anninghe and Zemuhe Faults slip left laterally at rates of 8 ± 2 mm/yr, which is consistent with the geodetic [e.g., *Shen et al*., 2005] result but ~3 mm/yr higher than the geological result [e.g., *Xu et al*., 2003]. We suggest that this difference results from distributed deformation across the Daliangshan subblock. The velocity profiles across other faults give similar results as that of the model-predicted slip rates. For more details, please refer to Figure 14. Geological slip rates, model-predicted slip rates, and velocity profile-derived slip rates are listed for comparison in Table 3. The overall good agreement between the geodetic and geologic slip rates suggests steady deformation rates consistent with results of *Shen et al*. [2005].

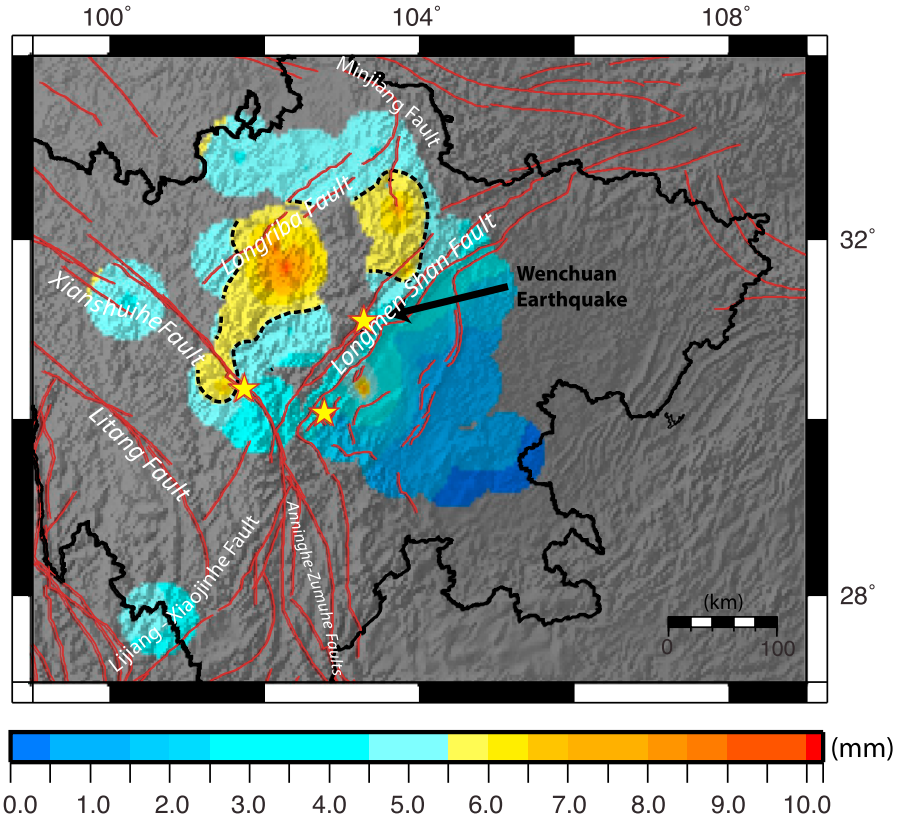

Figure 15. The magnitude of cumulative postseismic displacements detected in this study at GNSS/GPS stations after the 2008 Wenchuan event until 2015. Magnitudes are plotted for a 50 km radius around each station. Note the relatively higher postseismic signal in the eastern Tibetan Plateau outlined with a contour at 5.5 mm.

7.2. Resolved Deformation Zone

While conducting the statistical analysis for the kinematic models we found that some residual velocities appeared systematic, particularly in a region east of the Anninghe Fault where several large-magnitude earthquakes occurred in the past [*Sun et al.*, 2010]. We therefore performed additional tests to determine if our new velocity solution could be used to resolve more zones of deformation. In addition to the blocks described above we found two regions (Figure 8) where GNSS/GPS residuals are systematic. One region is located in easternmost of SC blocks (hereafter called Chenghai Block, CH), and the other is at the intersection area of the Longmen Shan and Anninghe Faults (hereafter called Mabian Block, MB). For each of these two blocks we evaluate the significance of the model fit by performing four groups of *F* tests: (1) use all of velocities described in section 3.3 and keep all faults locked, (2) use same velocities and allow fault to slip freely, (3) perform the same test as (1) but exclude sites 25 km along faults to mitigate effects from elastic strain accumulation except sites in CH and MB, and (4) same as (3) but keep faults freely slipping. Note that these tests are different from our previously described approach in sections 5.2 and 6 because we seek to resolve zones of deformation using all available data from our new, augmented GNSS/GPS velocity field.

Seven GNSS/GPS sites are within the CH Block domain. The four *F* test results are listed in Tables S3 and S4 in the supporting information, and it shows that, for all four cases, model fit improves significantly when the CH Block is included (confidence level $P_F > 95\%$). Twenty-one GNSS/GPS sites are in the MB Block domain. The *F* tests of four groups also show that adding the new MB Block improves the model fit significantly only with one exception—group 3 ($P_F = 90.1\%$). The estimated block rotation poles of these two blocks are provided in Table S5.

Historical records of seismic events and previously mapped faults also provide evidence of the CH and MB Blocks. It is reported that at least 11 historical events with $M_s > 6.0$ occurred along the fault bounding the

eastern side of MB Block. Similarly, for block CH there are also reports of historical events with $M_s > 6.0$ that occurred [*Sun et al*., 2010]. Prior to this study the kinematics of these blocks have not been well studied with GNSS/GPS data because of dense forest coverage [*Zhang*, 2013].

7.3. Constraints on the Spatial Extent of Viscoelastic Deformation in the Eastern Tibetan Plateau

Inverting our new interseismic GNSS/GPS velocity field describes rigid plate motions of the Sichuan Province with a reduced $\chi^2 = 0.48$. However, block rigidity is only achieved for blocks SPs and SPn after removing nearly all of the new continuous GNSS/GPS data in those regions because of their large misfit to the rigid block model. Therefore, velocities observed after the earthquake have no effect on the estimation of block rotations in the SPs and SPn blocks. Inverting postseismic data alone we can resolve rigid block motion for SPs, but the angular velocity vector (Table 2) is more than 5 times greater than block rotations derived from preseismic velocities. We propose that the continuous sites installed after the 2008 Wenchuan event in 2010 in blocks SPs and SPn (MAEK, SCMX, SCSP, SCXJ, KADN, MARK, HONY, and ABAZ) observe postseismic deformation related to viscoelastic relaxation. We estimate cumulative postseismic transient displacements for these continuous sites by computing the residual velocities compared to our new estimates of block angular rotations for SPs and SPn. We assume that the magnitude of the residual velocities represents cumulative displacements over the period of observations associated with postseismic deformation. This is a similar approach we used for the cumulative postseismic displacements at episodic sites shown in Figure 6. Displacements derived for the episodic sites are based on residuals from the interseismic velocity solution of *Zhang et al*. [2013]. We exclude velocities at GNSS/GPS sites associated with postseismic transient deformation from the final velocity solution provided in the supporting information.

Figure 15 shows that the magnitudes of horizontal displacements spanning post-Wenchuan to 2015 that we determine are associated with postseismic deformation. The spatial extent of postseismic deformation elucidated from GNSS/GPS data in this work extends up to 200 km west of the Beichuan into the eastern Tibetan Plateau. Cumulative postseismic displacements are relatively larger in magnitude and centered in a central region of the eastern margin of the Tibetan Plateau (Figure 15, yellow and red zones). The absolute magnitude of the displacement is less important than the relative magnitude because the amplitude of the signal will depend on the size of the earthquake. The location of the relatively higher magnitude postseismic displacements suggests a rheologic contrast in lithosphere of the eastern Tibetan Plateau that is consistent with hypothesized low-viscosity lower crust in this region [i.e., *Royden et al*., 1997; *Huang et al*., 2014]. This work resolves a broader zone of postseismic deformation than previously detected with interferometric synthetic aperture radar observations [*Huang et al*., 2014].

We resolve postseismic decay times of ~11 days for the deformation east of the Longmen Shan fault zone; however, it is not possible to constrain short-term decay times elsewhere in the region due to data availability. The observed transient signals west of the Longmen Shan are evidence of longer-term transients in the eastern Tibetan Plateau since the signal is present after 2010 at the continuous sites when data collection initiated. These longer-term transient signals further support a rheologically distinct lower crustal layer in the eastern Tibetan Plateau that is undergoing viscoelastic relaxation in response to the Wenchuan megathrust event.

8. Conclusions

We calculate a GNSS/GPS velocity field corrected for postseismic transient deformation using newly available continuous and episodic GNSS/GPS data spanning 2008–2015. We combine this velocity solution with interseismic velocities prior to the Wenchuan earthquake [*Zhang et al*., 2013] to provide an augmented secular velocity solution for the eastern Tibetan Plateau and Sichuan Basin as a contribution to the broader geophysical community. We then use it to revise the kinematics of the Sichuan Province providing new estimates of block rotations, evidence for two newly resolved blocks, and revised estimates of long-term slip rates on the Longmen Shan and surrounding active faults. The new kinematic model predicts fault slip rates that agree well with both geological and GNSS/GPS velocity profile-derived results, which indicates steady deformation rates of the region consistent with previous studies. Results from isolating postseismic transient deformation elucidates a broad region in the eastern margin of the Tibetan Plateau that supports models of lower crustal flow and extrusion tectonic hypotheses.

Acknowledgments

All data supporting the conclusions of this paper are available within the main body of the paper, in the supplementary section, and available as a data set published with this paper. We thank the Sichuan Surveying and Mapping Bureau and the Crustal Movement Observation Network of China for providing access to their data for publication in this manuscript. D.S. Stamps was funded, in part, by the NSF EAR Postdoctoral Fellowship program grant EAR1249295. X. Rui was funded, in part, by the CEA spark program XH15038. We thank B.H. Hager, L. Royden, and C. Burchfield for their insightful discussions about this work and R.W. King and T.A. Herring for answering the technical questions about GAMIT-GLOBK. We are also grateful for the comments by two anonymous reviewers and Associate Editor Yosuke Aoki, which have greatly improved this manuscript.

References

Altamimi, Z., L. Métivier, and X. Collilieux (2012), ITRF2008 plate motion model, *J. Geophys. Res.*, *117*, B07402, doi:10.1029/2011JB008930.

Bai, D., M. A. Meju, X. Ma, J. Teng, X. Kong, and M. Liu (2010), Crustal deformation of the eastern Tibetan Plateau revealed by magnetotelluric imaging, *Nat. Geosci.*, *3*(5), 358–362, doi:10.1038/ngeo830.

Calais, E., L. Dong, M. Wang, Z. Shen, and M. Vergnolle (2006), Continental deformation in Asia from a combined GPS solution, *Geophys. Res. Lett.*, *33*, L24319, doi:10.1029/2002JB002373.

Chen, Z., B. C. Burchfiel, Y. Liu, R. W. King, L. H. Royden, W. Tang, E. Wang, J. Zhao, and X. Zhang (2000), Global Positioning System measurements from eastern Tibet and their implications for India/Eurasia intercontinental deformation, *J. Geophys. Res.*, *105*, 16,215–16,227, doi:10.1029/2000JB900092.

Clark, M. K., J. W. M. Bush, and L. H. Royden (2005), Dynamic topography produced by lower crustal flow against rheological strength heterogeneities bordering the Tibetan Plateau, *Geophys. J. Int.*, *162*, 575–590, doi:10.1111/j.1365-246X.2005.02580.x.

Densmore, A. L., M. A. Ellis, Y. Li, R. Zhou, G. S. Hancock, and N. Richardson (2007), Active tectonics of the Beichuan and Pengguan faults at the eastern margin of the Tibetan Plateau, *Tectonics*, *26*, TC4005, doi:10.1029/2006TC001987.

Ding, K., C. Xu, and Y. Wen (2013), Postseismic deformation associated with the 2008 Wenchuan earthquake by GPS data [in Chinese], *Geomatics Inf. Sci. Wuhan Univ.*, *38*, 131–135.

Dong, D.-N., T. A. Herring, and R. W. King (1998), Estimating regional deformation from a combination of space and terrestrial geodetic data, *J. Geod.*, *72*, 200–214.

Du, P. S. (2000), Slip displacement and its rate about Zemuhe Fault [in Chinese], *Earthquake Res. Sichuan*, *1–2*, 49–64.

Dziewonski, A. M., T.-A. Chou, and J. H. Woodhouse (1981), Determination of earthquake source parameters from waveform data for studies of global and regional seismicity, *J. Geophys. Res.*, *86*, 2825–2852, doi:10.1029/JB086iB04p02825.

Ekström, G., M. Nettles, and A. M. Dziewonski (2012), The global CMT project 2004-2010: Centroid-moment tensors for 13,017 earthquakes, *Phys. Earth Planet. Inter.*, *200-201*, 1–9, doi:10.1016/j.pepi.2012.04.002.

England, P., and P. Molnar (2005), Late Quaternary to decadal velocity fields in Asia, *J. Geophys. Res.*, *110*, B12401, doi:10.1029/2004JB003541.

Flesch, L. M., A. J. Haines, and W. E. Holt (2001), Dynamics of the India–Eurasia collision zone, *J. Geophys. Res.*, *106*(B8), 16,435–16,460.

Gan, W., P. Zhang, Z.-K. Shen, Z. Niu, M. Wang, Y. Wan, D. Zhou, and J. Cheng (2007), Present-day crustal motion within the Tibetan Plateau inferred from GPS measurements, *J. Geophys. Res.*, *112*, B08416, doi:10.1029/2005JB004120.

He, H. L., and I. Yasutakyr (2007), Faulting on the Anninghe Fault zone, southwest China in late Quaternary and its movement model [in Chinese], *Acta Seismol. Sin.*, doi:10.1007/s11589-007-0571-4.

He, H. L., Z. J. Fang, and P. Li (1993), A preliminary approach to the fault activity of southern segment on Xiaojiang western branch fault [in Chinese], *J. Seismol. Res.*, *16*(3), 291–298.

He, H. L., F. M. Song, and C. Y. Li (1999), Topographic survey of micro faulted landform and estimation of strike slip rate for the Zemuhe Fault, Sichuan Province [in Chinese], *Seismol. Geol.*, *21*(4), 361–369.

He, H. L., I. Yasutaka, F. M. Song, and X. Q. Dong (2002), Late quaternary slip rate of the Xiaojiang Fault and its implication [in Chinese], *Seismol. Geol.*, *24*(1), 14–25.

He, H. L., H. L. Ran, and I. Yasutaka (2006), Uniform strike-slip rate along the Xianshuihe-Xiaojiang fault system and its implications for active tectonics in southeastern Tibet [in Chinese], *Acta Geol. Sin.*, *80*(3), 376–386, doi:10.1111/j.1755-6724.2006.tb00255.x.

Herring, T. A., R. W. King, and S. C. McClusky (2010a), Documentation of the MIT GPS analysis software: GAMIT release 10.4 Mass. Inst. of Technol., Cambridge.

Herring, T. A., R. W. King, and S. C. McClusky (2010b), GLOBK: Global Kalman filter VLBI and GPS analysis program, release 10.4, Mass Instit. of Technol., Cambridge.

Huang, M. H., R. Burgmann, and A. M. Freed (2014), Probing the lithospheric rheology across the eastern margin of the Tibetan Plateau, *Earth Planet. Sci. Lett.*, *396*, 88–96, doi:10.1016/j.epsl.2014.04.003.

Hubbard, J., and J. H. Shaw (2009), Uplift of the Longmen Shan and Tibetan Plateau, and the 2008 Wenchuan ($M = 7.9$) earthquake, *Nature*, *458*(7235), 194–197, doi:10.1038/nature07837.

Ji, K. H. (2011), Transient signal detection using GPS position time series PhD thesis, 243 pp., Mass. Inst. of Technol., Cambridge, 20 July.

Ji, K. H., and T. A. Herring (2011), Transient signal detection using GPS measurements: Transient inflation at Akutan Volcano, Alaska, during early 2008, *Geophys. Res. Lett.*, *38*, L06307, doi:10.1029/2011GL046904.

Jiang, Z., M. Wang, Y. Wang, Y. Wu, S. Che, Z. K. Shen, and Q. Li (2014), GPS constrained coseismic source and slip distribution of the 2013 M_w6.6 Lushan, China, earthquake and its tectonic implications, *Geophys. Res. Lett.*, *41*, 407–413, doi:10.1002/2013GL058812.

King, R. W., F. Shen, B. C. Burchfiel, L. H. Royden, E. Wang, Z. Chen, Y. Liu, X.-Y. Zhang, J.-X. Zhao, and Y. Li (1997), Geodetic measurement of crustal motion in southwest China, *Geology*, *25*, 179–182, doi:10.1002/2013GL058812.

Larson, K. M., and D. C. Agnew (1991), Application of the global positioning system to crustal deformation measurement, 1. Precision and accuracy, *J. Geophys. Res.*, *96*(B10), 16,547–16,565, doi:10.1029/91JB01275.

Laske, G., G. Masters, Z. Ma, and M. E. Pasyanos (2012), CRUST1.0: An updated global model of the Earth's crust EGU General Assembly, 14, p. 3743.

Li, C., R. D. van der Hilst, E. R. Engdahl, and S. Burdick (2008), A new global model for *P*-wave speed variations in Earth's mantle, *Geochem. Geophys. Geosyst.*, *9*, doi:10.1029/2007GC001806.

Li, S., W. D. Mooney, and J. Fan (2006), Crustal structure of mainland China from deep seismic sounding data, *Tectonophysics*, *420*(1), 239–252, doi:10.1016/j.tecto.2006.01.026.

Li, T. S., and Q. F. Du (1989), Horizontal displacement and earthquake recurrence along Luhuo segment of the Xianshuihe fault zone [in Chinese], *Seismol. Geol.*, *11*(4), 31–42.

Li, T., Q. Du, and Z. You (1997), *The Active Xianshuihe Fault Zone and Seismic Risk Assessment* [in Chinese], *Cartogr. Publ.*, House of Chengdu, Chengdu, China.

Li, Z., B. Tian, S. Liu, and J. Yang (2013), Asperity of the 2013 Lushan earthquake in the eastern margin of Tibetan Plateau from seismic tomography and aftershock relocation, *Geophys. J. Int.*, *195*(3), 2016–2022, doi:10.1093/gji/ggt370.

Liu, Q. Y., R. D. van der Hilst, Y. Li, H. J. Yao, J. H. Chen, B. Guo, S. H. Qi, J. Wang, H. Huang, and S. C. Li (2014), Eastward expansion of the Tibetan Plateau by crustal flow and strain partitioning across faults, *Nat. Geosci.*, *7*(5), 361–365, doi:10.1038/ngeo2130.

Liu-Zeng, J., et al. (2009), Co-seismic ruptures of the 12 May 2008, M_s 8.0 Wenchuan earthquake, Sichuan: East–west crustal shortening on oblique, parallel thrusts along the eastern edge of Tibet, *Earth Planet. Sci. Lett.*, *286*, 355–370, doi:10.1016/j.epsl.2009.07.017.

Loveless, J. P., and B. J. Meade (2011), Partitioning of localized and diffuse deformation in the Tibetan Plateau from joint inversions of geologic and geodetic observations, *Earth Planet. Sci. Lett.*, *303*(1), 11–24, doi:10.1016/j.epsl.2010.12.014.

Ma, B. Q., G. Su, Z. H. Hou, and S. B. Shu (2005), Late quaternary slip rate in the central part of the Longmenshan fault zone from terrace deformation along the Minjiang River [in Chinese], *Seismol. Geol.*, *27*(2), 234–242.
McCaffrey, R. (2005), Block kinematics of the Pacific-North America plate boundary in the southwestern US from inversion of GPS, seismological, and geologic data, *J. Geophys. Res.*, *110*, B07401, doi:10.1029/2004JB003307.
McCaffrey, R. (2009), Time-dependent inversion of three-component continuous GPS for steady and transient sources in northern Cascadia, *Geophys. Res. Lett.*, *36*, L07304, doi:10.1029/2008GL036784.
McCaffrey, R., A. I. Qamar, R. W. King, R. Wells, G. Khazaradze, C. A. Williams, C. W. Stevens, J. J. Vollick, and P. C. Zwick (2007), Fault locking, block rotation and crustal deformation in the Pacific Northwest, *Geophys. J. Int.*, *169*, 1315–1340, doi:10.1111/j.1365-246X.2007.03371.x.
McClusky, S., et al. (2000), Global Positioning System constraints on plate kinematics and dynamics in the eastern Mediterranean and Caucasus, *J. Geophys. Res.*, *105*, 5695–5719, doi:10.1029/1999JB900351.
Meade, B. J. (2007), Present-day kinematics at the India-Asia collision zone, *Geology*, *35*(1), 81–84, doi:10.1130/G22924A.1.
Medvedev, S. and C. Beaumont (2006), Growth of continental plateaus by channel injection: Models designed to address constraints and thermomechanical consistency, in *Channel Flow, Ductile Extrusion and Exhumation in Continental Collision Zones*, edited by R. D. Law, M. P. Searle, and L. Godin, pp., 147–164, Geol. Soc. London, London, doi:10.1144/GSL.SP.2006.268.01.06
Pei, S., H. Zhang, J. Su, and Z. Cui (2014), Ductile gap between the Wenchuan and Lushan earthquakes revealed from the two-dimensional Pg seismic tomography, *Sci. Rep.*, *4*, doi:10.1038/srep06489.
Press, W. H., B. P. Flannery, S. A. Teukolsky, and W. T. Vetterling (1989), *Numerical recipes*, 502 pp., Cambridge Univ. Press.
Qian, H. (1989), Faulted Landforms along the Xianshuihe fault zone and their seismological significance [in Chinese], *Acta Seismol. Sin.*, *11*(4), 43–49.
Qian, H., Z. L. Luo, and X. Z. Wen (1990), Preliminary study of characteristic earthquakes in the Xianshui fault zone [in Chinese], *Acta Seismol. Sin.*, *12*(1), 22–29.
Ran, H. L., and H. L. He (2006), Research on the magnitude and recurrence interval of characterized earthquakes with magnitude ≥6.7 along the northwestern portion of the Xianshuihe fault zone in western Sichuan, China [in Chinese], *Chin. J. Geophys.*, *49*(1), 153–161, doi:10.1002/cjg2.821.
Ran, Y. H., J. W. Cheng, H. L. Gong, and L. C. Chen (2008), Late quaternary geomorphic deformation and displacement rates of the Anninghe Fault around Zimakua [in Chinese], *Seismol. Geol.*, *30*(1), 86–98.
Ran, Y., L. Chen, J. Chen, H. Wang, G. Chen, J. Yin, X. Shi, C. Li, and X. Xu (2010), Paleoseismic evidence and repeat time of large earthquakes at three sites along the Longmenshan fault zone, *Tectonophysics*, *491*, 141–153.
Reilinger, R., et al. (2006), GPS constraints on continental deformation in the Africa-Arabia-Eurasia continental collision zone and implications for the dynamics of plate interactions, *J. Geophys. Res.*, *111*, B05411, doi:10.1029/2005JB004051.
Ren, J. W. (1990), Preliminary study on the recurrence period of strong earthquakes on the fracture zone of Zemuhe, west of Sichuan [in Chinese], *Inland Earthquake*, *4*(2), 107–115.
Ren, J. W. (1994), Late quaternary displacement and slip rate of Zemuhe Fault in Sichuan, China [in Chinese], *Seismol. Geol.*, *16*(2), 146.
Royden, L. H., B. C. Burchfiel, R. W. King, E. Wang, Z. L. Chen, F. Shen, and Y. P. Liu (1997), Surface deformation and lower crustal flow in eastern Tibet, *Science*, *276*, 788–790.
Savage, J. C., and R. O. Burford (1970), Accumulation of tectonic strain in California, *Bull. Seismol. Soc. Am.*, *60*, 1877–1896.
Savage, J. C., J. L. Svarc, and S. B. Yu (2005), Postseismic relaxation and transient creep, *J. Geophys. Res.*, *110*(B11), doi:10.1029/2005JB003687.
Shen, J., and Y. P. Wang (1999), Estimation of seismic risk of the Xiaojiang active fault zone using slip rate [in Chinese], *J. Seismol. Res.*, *22*(3), 251–259.
Shen, J., Y. P. Wang, F. M. Song, W. X. Yu, Z. Q. Cao, X. Y. Hou, X. H. Shen, and Z. X. Li (1998), The evolution stages of the late Cenozoic tectonic basins in the central part of the Xiaojiang fault zone [in Chinese], *J. Seismol. Res.*, *21*(1), 58–64.
Shen, Z. K., J. Lü, M. Wang, and R. Burgmann (2005), Contemporary crustal deformation around the southeast borderland of the Tibetan Plateau, *J. Geophys. Res.*, *110*, B11409, doi:10.1029/2004JB003421.
Shen, Z.-K., J. Sun, P. Zhang, Y. Wan, M. Wang, R. Bürgmann, Y. Zeng, W. Gan, H. Liao, and Q. Wang (2009), Slip maxima at fault junctions and rupturing of barriers during the 12 May 2008 Wenchuan earthquake, *Nat. Geosci.*, *2*, 718–724, doi:10.1038/ngeo636.
Song, F. M., Y. P. Wang, J. Shen, Z. Q. Cao, and X. H. Shen (1997), The development stages of the basins along the middle segment of the Xiaojiang fault zone and its relation to regional tectonic movement [in Chinese], *Seismol. Geol.*, *19*(3), 211–217.
Stein, S., and R. G. Gordon (1984), Statistical tests of additional plate boundaries from plate motion inversions, *Earth Planet. Sci. Lett.*, *69*(2), 401–412.
Sun, C. M., L. Wang, and W. Xie (2010), Compilation of Sichuan historical earthquakes volume 1 [in Chinese] Sichuan Peoples Publishing House.
Tang, W. Q., Y. P. Liu, Z. L. Chen, Q. Z. Zhang, and J. X. Zhao (2004), The preliminary study of the tectonic activities along the boundary faults around the Minshan uplift, western Sichuan [in Chinese], *Sediment. Geol. Tethyan Geol.*, *24*(4), 31–34.
Tapponnier, P., Z. Q. Xu, F. Roger, B. Meyer, N. Arnaud, G. Wittlinger, and J. S. Yang (2001), Oblique stepwise rise and growth of the Tibet Plateau, *Science*, *294*, 1671–1677.
Taylor, M., and A. Yin (2010), Active structures of the Himalayan-Tibetan orogen and their relationships to earthquake distribution, contemporary strain field, and Cenozoic volcanism, *Geosphere*, *5*, 199–214, doi:10.1130/GES00217.1.
Thatcher, W. (2007), Microplate model for the present-day deformation of Tibet, *J. Geophys. Res.*, *112*, B01401, doi:10.1029/2005JB004244.
Unsworth, M. J., A. G. Jones, W. Wei, G. Marquis, S. G. Gokarn, J. E. Spratt, P. Bedrosian, B. Roberts, and Team* (2005), Crustal rheology of the Himalaya and southern Tibet inferred from magnetotelluric data, *Nature*, *438*(7064), 78–81, doi:10.1038/nature04154.
Wang, C., W. Chan, and W. Mooney (2003), Three-dimensional velocity structure of crust and upper mantle in southwestern China and its tectonic implications, *J. Geophys. Res.*, *108*, 176–193, doi:10.1029/2002JB001973.
Wang, H., J. Liu, Y. L. Shi, H. Zhang, and G. M. Zhang (2008), Dynamic simulation of strong earthquakes in the Xianshuihe fault zone [in Chinese], *Sci. China, Ser. D*, *38*(7), 808–818.
Wang, X. M., C. G. Zhang, and X. Y. Pei (1998), Structural activity and evolution since the late Quaternary on Anninghe Faults [in Chinese], *Earthquake Res. China*, *98*(4), 1–12.
Wen, X. Z. (1990), Conditional probabilities for the recurrence of earthquakes on the Xianshuihe fault zone within the coming three decades [in Chinese], *Earthquake Res. China*, *6*(4), 8–16.
Wen, X. Z. (1993), Estimation of rupture segments and potential seismic hazard of Xiaojiang fault zone [in Chinese], *Acta Sesmol. Sin.*, *15*(3), 322–330.
Wen, X. Z. (2000), Character of rupture segmentation of the Xianshuihe-Anninghe-Zemuhe fault zone, western Sichuan [in Chinese], *Seismol. Geol.*, *22*(3), 239–249.
Wen, X. Z., C. R. Allen, and L. Zhuo (1989), Segmentation, geometric features, and their seismotectonic implications for the Holocene Xianshuihe fault zone [in Chinese], *Acta Seismol. Sin.*, *11*(4), 362–372.

Wen, X. Z., S. L. Ma, and X. L. Lei (2007), Newly found surface rupture remains of large historical earthquakes on and near the transition segment of the Anninghe and Zemuhe fault zones western Sichuan [in Chinese], *Seismol. Geol.*, *29*(4), 826–833.
Wen, X. Z., F. Du, and G. Yi (2013), Earthquake potential of the Zhaotong and Lianfeng fault zones of the eastern Sichuan-Yunnan border region [in Chinese], *Chin. J. Geophys.*, *56*(10), 3361–3372, doi:10.6038/cjg20131012.
Wu, Y., Z. Jiang, M. Wang, S. Che, H. Liao, Q. Li, and X. Liu (2013), Preliminary results pertaining to coseismic displacement and preseismic strain accumulation of the Lushan M_s 7.0 earthquake, as reflected by GPS surveying [in Chinese], *Chin. Sci. Bull.*, *58*(28–29), 3460–3466.
Xiang, H. F., X. W. Xu, S. M. Guo, W. X. Zhang, H. W. Li, and G. H. Yu (2002), Sinistral thrusting along the Lijiang-Xiaojinghe Fault since Quaternary and its geologic-tectonic significance [in Chinese], *Seismol. Geol.*, *24*(3), 188–198.
Xu, L., S. Rondenay, and R. D. Van der Hilst (2007), Structure of the crust beneath the southeastern Tibetan Plateau from teleseismic receiver functions, *Phys. Earth Planet. Inter.*, doi:10.1016/j.pepi.2007.09.002.
Xu, X. W., X. Wen, R. Zheng, W. Ma, F. Song, and G. Yu (2003), Pattern of latest tectonic motion and dynamics of faulted blocks in Yunnan and Sichuan [in Chinese], *Sci. China, Ser. D*, *33*(suppl), 151–162.
Xu, X. W., P. Z. Zhang, X. Z. Wen, and Z. L. Qin (2005), Features of active tectonics and recurrence behaviors of strong earthquakes in the western Sichuan Province and its adjacent regions [in Chinese], *Seismol. Geol.*, *27*(3), 446–461.
Xu, X. W., X. Wen, G. Yu, G. Chen, Y. Klinger, J. Hubbard, and J. Shaw (2009), Coseismic reverse- and oblique-slip surface faulting generated by the 2008 M_w 7.9 Wenchuan earthquake, China, *Geology*, *37*, 515–518, doi:10.1130/G25462A.1.
Yao, H., R. D. van der Hilst, and M. V. de Hoop (2006), Surface-wave array tomography in SE Tibet from ambient seismic noise and two-station analysis: I—Phase velocity maps, *Geophys. J. Int.*, *166*, 732–744, doi:10.1111/j.1365-246X.2006.03028.x.
Yao, H., C. Beghein, and R. D. van der Hilst (2008), Surface-wave array tomography in SE Tibet from ambient seismic noise and two-station analysis: II—Crustal and upper mantle structure, *Geophys. J. Int.*, *173*, 205–219, doi:10.1111/j.1365-246X.2007.03696.x.
Yi, G. X., J. Fan, and X. Z. Wen (2005), Study on faulting behavior and fault-segments for potential strong earthquake risk along the central-southern segment of Xianshuihe fault zone based on current seismicity [in Chinese], *Earthquakes*, *25*(1), 58–66.
Zhang, P. Z. (2008), The co-seismic surface displacement of the great Wenchuan earthquake of May 12, 2008, Sichuan, China, from GPS measurements [in Chinese], *Chin. Sci.*, *38*(10), 1195–1206.
Zhang, P. Z. (2013), A review on active tectonics and deep crustal processes of the western Sichuan region, eastern margin of the Tibetan Plateau, *Tectonophysics*, *584*, 7–22, doi:10.1016/j.tecto.2012.02.021.
Zhang, P. Z., et al. (2004), Continuous deformation of the Tibetan Plateau from Global Positioning System data, *Geology*, *32*, 809–812, doi:10.1130/G20554.1.
Zhang, P. Z., X. Z. Wen, Z. K. Shen, and J. H. Chen (2010), Oblique high-angle listric-reverse faulting and associated straining processes: The Wenchuan earthquake of 12 May 2008, Sichuan, China, *Annu. Rev. Earth Planet. Sci.*, *38*, 353–382.
Zhang, S. M., and F. R. Xie (2001), Seismo-tectonic divisions of strong earthquakes ($M_s \geq 7.0$) and their tectonic geomorphology along Xianshuihe-Xiaojiang fault zone [in Chinese], *Acta Seismol. Sci.*, *23*(1), 36–44.
Zhang, Z. Q., R. McCaffrey, and P. Zhang (2013), Relative motion across the eastern Tibetan Plateau: Contributions from faulting, internal strain and rotation rates, *Tectonophysics*, *584*, 240–256, doi:10.1016/j.tecto.2012.08.006.
Zhao, X. L., Q. D. Deng, and S. F. Chen (1994), Tectonic geomorphology of the Minshan uplift in western Sichuan, southwestern China [in Chinese], *Seismol. Geol.*, *16*(4), 429–439.
Zhou, R. J., X. H. Pu, Y. L. He, X. G. Li, and T. Y. Ge (2000), Recent activity of Minjiang fault zone, uplift of Minshan block and their relationship with seismicity of Sichuan [in Chinese], *Seismol. Geol.*, *22*(3), 285–294.
Zhou, R. J., Y. L. He, T. Yang, Q. He, and X. G. Li (2001), Slip rate and strong earthquake rupture on the Moxi-Mianning segment along the Xianshuihe-Anninghe fault zone [in Chinese], *Earthquake Res. China*, *17*(3), 253–262.
Zhou, R. J., Y. Q. Ye, Y. Li, X. G. Li, Y. L. He, and T. Y. Ge (2007), Late-Quaternary activity of the Shawan segment of the Litang Fault [in Chinese], *Quat. Sci.*, *27*(1), 45–53.